# Test Study and Analysis of Accumulated Permanent Axial Strain of a Subgrade Fill under Cyclic High-Speed Railway Loading

By

Wen-Bo CHEN, Ph.D. Candidate
Department of Civil and Environmental Engineering, The Hong Kong Polytechnic University, Kowloon, Hong Kong, China (Email: 13900710R@connect.polyu.hk)

Jian-Hua YIN, Ph.D., Chair Professor
Department of Civil and Environmental Engineering, The Hong Kong Polytechnic University, Kowloon, Hong Kong, China (Email: cejhyin@polyu.edu.hk)

Wei-Qiang FENG, Ph.D.
Department of Civil and Environmental Engineering, The Hong Kong Polytechnic University, Kowloon, Hong Kong. China (Email: 11901182r@connect.polyu.hk)

Lalit BORANA, Ph.D.
Department of Civil and Environmental Engineering, The Hong Kong Polytechnic University, Kowloon, Hong Kong. China (Email: lalitborana@gmail.com)

Ren-Peng CHEN, Professor
School of Civil Engineering and Architecture, Zhejiang University, Zheda Road 38#, Hangzhou 310027, China (Email: chenrp@zju.edu.cn)

September 2017

Manuscript submitted to International Journal of Geomechanics for possible publication as a Technical Paper

**ABSTRACT:** The ballastless track system (BTS) is widely adopted in the construction of High-Speed Railway (HSR), wherein the vehicle induced cyclic stresses are evenly transferred to subgrade at a smaller amplitude, as compared to the conventional ballast track system. In this study, both static and cyclic triaxial tests were performed on a subgrade fill that is procured from an HSR construction site in Mainland China. The subgrade fill contains high fine content ($d < 0.075$ mm). The static tests yield the stress-strain-strength relationship and provide a reference for the cyclic tests. In this study, the permanent axial strain and resilient modulus under cyclic HSR loading are studied based on the stress levels in the field. Based on the test data, a new empirical equation is proposed to predict the accumulated permanent axial strain with cycle number and low cyclic deviator stress. A new method for determining all parameters in this equation is proposed and testified by fitting test data. The results show that the prediction from newly proposed relationship are in good agreement with the experimental results. The resilient behavior of the fill under cyclic loading is also investigated. It is found that under low-stress levels, the resilient modulus slightly decreases with the increase of stresses, which is not well described by the existing models.

**KEYWORDS:** High-Speed Railway, subgrade, static compression, cyclic loading, permanent axial strain, resilient modulus.

## INTRODUCTION

The construction of High-Speed Rail (HSR) boomed in last decade in China. The engineers adopt ballastless track system rather than ballast track system to meet the high operational requirements of HSR regarding smoothness, safety, and durability. The ballast track system has many merits, such as the convenience in installation, low construction expenses, and the drainage ability. However, the abrasion or even crushing of ballast, plus the gradual decrease in confining pressure results in uneven sleeper support and excessive settlement (Indraratna et al. 2005; Thakur et al. 2013). Whereas, the ballastless track possesses advantages regarding accessibility of material, high durability, less maintenance expense, and long service life cycle (Indraratna et al. 2011). The cross-section drawing of track bed is shown in Figure 1. The surface layer is normally well-graded gravels which are well compacted and cause little settlements. The bottom is the ground which is normally stiff soils or bedrock that cause little settlements. In case, the ground soils are not competent, bridges or embankment with pile foundations or other ground improvement treatment techniques are normally used (Chen et al. 2009; Jiang et al. 2014; Zhao et al. 2016). The Type A and Type B fills (Ye 2004) are classified by the particle size distribution, particle shape, and fine content. The improved soils should possess the equivalent stiffness and strength with those of Type A and Type B fills. The coarse-grained aggregate, like well-graded crushed rock, natural pebble or sand gravel, is recommended as the material of subgrade. Normally the fine content of the bottom layer of the subgrade is larger than that of the top layer.

To investigate the resilient modulus, $M_r$, and permanent axial strain, $\Delta\varepsilon_{ap}$, of coarse-grained aggregate, researchers conducted numerous cyclic triaxial tests (Monismith et al. 1967; Hicks and Monismith 1971; Barksdale and Itani 1989; Lekarp and Dawson 1998; Lackenby et al. 2007; Thakur et al. 2013). However, the majority of them were aimed to study the dynamic

behavior of subgrade of ballast track under high cyclic deviator stress, and low fine content, which is not the common case for the ballastless track system.

It is widely accepted that stress state is the most significant influencing factor on the resilient and permanent strain behavior. The particles in the top layer of subgrade mainly may be integrated by interlocking and friction among each other. The deformation in this layer under dynamic loading is due to rearrangement of particles when the stress level is low and reaches to a stable state. However, when the stress level is high, relative displacement occurs between particles and abrasion happen on the part of them, which may result in larger and unstable deformation. The particles in the bottom layer of subgrade are mainly integrated by friction and cohesion since it contains a higher content of fine particles. Under normal circumstances, the concrete slabs, which are of high stiffness, mitigate significantly and distribute evenly the high dynamic load transferred from train wheel to subgrade part. Qu et al. (2012) recorded that the vertical dynamic stress markedly decreased from 18 kPa at the surface of subgrade to 2 kPa at the bottom of subgrade when the high-speed train was running at a speed of 350 km/h. Zhan and Jiang (2010) also found that the vertical dynamic stress at the top surface of the subgrade is lower than 10 kPa when train's speed is 220 km/h. Besides, Guo (2012) estimated that the effective confining pressure of subgrade ranged from 20 kPa to 100 kPa with the increase of depth. Nevertheless, it is possible that dynamic stress reaches to a high level if the track system is not well maintained like uneven settlement develops or cracking in rail occurs. Therefore, the study of subgrade of ballastless track system should not only focus on the dynamic strength of the subgrade but also, with a higher level of attention, on the dynamic response of subgrade under low dynamic stress.

Accurately predicting the permanent strain is a complex issue due to several factors and uncertainties associated with soil parameters. Many researchers (Raymond and William, 1978;

92 Thom 1988) proposed to relate it with the ratio of peak cyclic stress to the ultimate shear strength
93 of the material. However, Lekarp and Dawson (1998) argued that permanent strain development
94 be a gradual process, rather than a sudden collapse as in static failure tests. When the cyclic
95 deviator stress is high, the deformation processes contain crushing and overriding of large particles.
96 Nevertheless, when the stress or strain level is far away from those at failure, the deformation of
97 big particles consists primarily of the elastic deformation of particles themselves and sliding. If
98 the fine content is high, the effect of the fine particles is more dominant on deformation (Yideti et
99 al. 2013). Regarding resilient behavior, well-fitted curves considering the whole range of stress
100 levels may also hide the behavior of specimen under small stress.

101 In this study, three static compression tests were conducted on the soils to obtain the stress-
102 strain-strength relationship. Also, a series of cyclic triaxial tests were performed to investigate the
103 long-term permanent strain development, and the resilient behavior of the subgrade soils under
104 various stress states. A new empirical equation is proposed to predict the accumulated permanent
105 axial strain with cycle number under low cyclic deviator stress.
106

107 **EXPERIMENTAL PROGRAMME**

108 ***Materials and Testing Apparatus***

109 The authors adopted the fill in the bottom layer of subgrade, which was procured from a
110 construction site in Zhejiang Province, China, as the testing material. According to the Chinese
111 code for design of HSR (TB 10020 2009), the height of the bottom layer of the subgrade is 2.3 m,
112 which accounts for more than half of the total height and contributes significantly to the total
113 settlement of subgrade. Importantly, the content of fines of the bottom layer of subgrade could be
114 up to 30 %. The AASHTO T 307-99 (2007) recommended a ratio between the triaxial specimen

diameter and the maximum particle size should not be smaller than 5. However, Vallerga et al. (1975) recommended that the ratio of 3-4 times be sufficient for the cyclic triaxial tests. To reflect the real behavior of soils and decrease the possible discrepancy of testing data, the maximum particle size of 26.5 mm was determined. For a specimen with a diameter of 100 mm, the ratio between the specimen diameter and the maximum particle size is 3.77. The initial and scaled-down particle size distribution curves are presented in Figure 2. The particles with diameters larger than 26.5 mm were removed. The scaling down method may change the behavior of the material slightly. It is still valuable and significant to study the cyclic response of the subgrade soils. Moreover, the basic characteristics of soils are listed in Table 1.

The loading frame is a sophisticated servo-controlled HCA-100 system (GCTS, USA), and possess the loading frequency up to 20 Hz. All the transducers were calibrated before the tests were performed.

***Testing Scheme***

The testing scheme is shown in Table 2. The denotations, S, and D, mean static compression tests and cyclic loading tests, respectively. The sketch of stress path and the definitions of the variables in cyclic tests are shown in Figure 3. In the static compression tests, three levels of effective confining pressure, $\sigma_3'$, (20, 50, 100 kPa) were chosen according to the field stress condition (Guo, 2012). In cyclic compression tests, nine specimens experienced nine pair-wise combinations of three effective confining pressures (20, 50 100 kPa) and three amplitudes of cyclic deviator stress, $\Delta q_{cyc}$, (10, 25, 40 kPa). Three sets of stepwise increasing cyclic deviator stress were applied on three specimens under the same effective confining pressures as those in the previous tests. To investigate the relationship between static and cyclic test results,

a quantitative parameter, $\Delta q_{cyc} / \Delta q_{sta,f}$, is defined as the ratio of the amplitude of cyclic deviator stress, and the difference between the peak cyclic deviator stress and the deviator stress in the anisotropic consolidation. In the first 12 tests, the ratios between the effective major principal stress and the effective minor principal stress ($\sigma_1'/\sigma_3'$) are 2, which means that all the specimens were consolidated under anisotropic stress state. The last specimen (i. e. RM_Sat) was tested under various stress states to investigate the resilient response. It was consolidated under six effective confining pressures (20, 50, 75, 100, 150, 200 kPa), for each, there are four principal stress ratios (1, 1.25, 1.5 and 2). As shown in Figure 4, 24 consolidation stress states were presented and they were applied successively along the direction of arrows. To avoid the excessive deformation from occurring, when $\sigma_3'$ is 20 kPa, only four cyclic deviator stresses (10, 20, 30, and 50 kPa) were applied in sequence for each consolidation stress state. Also, when $\sigma_3'$ is 50 kPa, the cyclic deviator stresses of 10, 20, 30, 50 and 70 kPa were applied for each consolidation stress state. Six levels of cyclic deviator stress were applied for the remaining consolidation stress states. The cycle number is 100 for each. In total, 132 values of resilient modulus were produced under 132 stress states.

***Testing Procedures***

The test procedures are divided into two sections: a) preparation of specimen and b) applying stress state.

(a) The preparations of soil specimens are the same for static and cyclic loading tests, which includes mixing oven-dried soil with water, compaction of soil specimen, and set-up of soil specimen. All the soils were firstly kept in the oven at a temperature of 105 °C for overnight. After that, the required amount of soils were prepared according to scaled-down soil

particle distribution curve. Then the dry soils were put in a mixing bowl, and the calculated amount of distilled water was added. The mixing bowl with wet soil was sealed with preservative film and put in a room under a constant temperature of 20 °C for 24 hours. Continuous monitoring of the water content was conducted during this process, and more water was added if the water content was below the required value. Before compaction, the soil was mixed thoroughly so that the water content was achieved evenly in the mixed soil specimen (Borana et al. 2015). The soil specimens were directly compacted in 5 equal layers, on the bottom platen inside a split mold using an electrical rotary hammer (TE 7-C, Hilti). Continuous monitoring of the change of distance between top brim of mold and the top surface of soil specimen was done to ensure the height of each layer is identical to the target height. The densities of every specimen were controlled around $95 \pm 1\%$ of the maximum dry density, i.e., $2085.7 \pm 22.0$ kg/m$^3$.

(b) Soil specimens were saturated using back pressure saturation method. After that, they experienced isotropic and then anisotropic consolidation states. All the specimens were loaded under drained condition. In the static compression tests, specimens were sheared at a constant strain rate of 0.33 mm/min (BS 1377:1990) under drained condition.Generally, the distance between two axles or bogies is 20 m, and the speed of High-speed train can be up to 350 km/h. Therefore, the frequency of cyclic loading is estimated by dividing the distance by speed, i.e., $f$ = 4.86 Hz. In this study, a sine wave of 5 Hz was adopted in the investigation of permanent strain. According to AASHTO T 307-99 (2007), 1 Hz was chosen as the loading frequency for resilient response tests. Before all the resilient tests were conducted, the specimen experienced a conditioning period with 500 loading cycles under an effective confining pressure of 50 kPa and the cyclic deviator stress of 30 kPa to

create good contacts between specimen and platens. Necessary corrections, such as the uplift force of loading piston, membrane restraining effect, and penetration, and the variation of sample dimensions, were all considered in the data analysis. The photos of tested specimens are presented in Figure 5. It is noted that membrane penetration correction was done on all data from the tests since the particles are relatively large (Baldi and Nova 1984).

## RESULTS AND DISCUSSIONS

### *Static Compression Tests*

A series of static compression tests were conducted to understand the basic static stress-strain-strength behavior of the fill. This is used as a reference to explain the dynamic performance of the material when the same fill is subjected to cyclic loading.

Figure 6(a) shows the plot of deviator stress versus axial strain under three different effective confining pressures. The starting points of deviator stress are not on the origins of coordinates since the specimens were all consolidated under anisotropic stress state with $K_0 = 0.5$, where $K_0$ is the ratio between effective confining pressure and effective axial stress. It is seen from Figure 6(a) that the deviator stress increases rapidly in the initial compression stage and the rate of increase is higher when effective confining pressure is greater. The strain softening phenomenon is observed when effective confining pressures are small, i.e., 20 and 50 kPa. This is because that for highly compacted soil specimens, particles would roll over the nearby particles without significant crushing under a low confining pressure. Further, the deviator stresses increase again which is probably because a new stable particle skeleton structure was achieved after particle movement. It is observed that no obvious softening phenomenon occurs when the effective

confining pressure is 100 kPa. This behavior reflects that the higher confining pressure suppresses particles from moving and overriding. Moreover, several sudden drops can be observed, which should be owing to sudden internal movement of particles, especially for particles with sharp corners and possible breakage of the sharp corners of the particles in which the contact stress is larger than the strength of particles.

Figure 6(b) presents the relationships between mean effective stress ($p'$) and deviator stress ($q$). The static strength envelope is depicted by fitting three points at which three specimens arrive at peak deviator stresses ($q_{sta,f}$). The apparent effective friction angle, $\phi'$, and the apparent effective cohesion could be calculated as 47.6 ° and 9.83 kPa respectively. It shall be pointed out that this cohesion is not the true cohesion, rather than the interception at the zero mean effective stress point by a line fitting to the non-linear failure envelope. In fact, due to particle interlocking, the peak failure points form a nonlinear failure envelope with zero effective cohesion.

Figure 6(c) demonstrates the relationships between the variations of stress ratio ($q/p'$) and axial strain. This figure shows that stress ratio moves toward a constant value of 2 with the increase of axial strain, irrespective of the effective confining pressure. The relationship between void ratio and the mean effective stress is in Figure 6(d). The volumetric strains of three specimens exhibit a phase transition, i.e., change from shear compression to shear dilation. The dilation becomes more significant when the effective confining pressure gets lower, which again proves that higher effective confining pressure restrains particle movement. In the view of practical construction, well-constructed restraints at two lateral sides of the subgrade are mandatory to prevent an occurrence of excessive volumetric change. Moreover, all the curves approach to the critical state, which is expressed by a straight line in the semi-logarithmic scale.

***Permanent Strain Behavior in Cyclic Compression Tests***

Figure 7 shows the relationships between permanent axial strain accumulated and cycle number under three low cyclic deviator stresses (10, 25, 40 kPa) and three effective confining pressures (20, 50, 100 kPa) in the semi-logarithmic scale. As expected, the higher effective confining pressure increases the deformation resistance of specimens.

It is noted that for every effective confining pressure, a higher cyclic deviator stress ($\Delta q_{cyc}$) aggravates the development of the permanent axial strain. Moreover, this aggravation becomes more significant with the increase of the cyclic deviator stress. Take the specimens under an effective confining pressure of 20 kPa for an example, the final permanent axial strain is increased from 0.1% to 0.129% by a growth rate of 29% when the cyclic deviator stress is increased from 10 kPa to 25 kPa, and from 0.1% to 0.203% by a growth rate of 103% when the cyclic deviator stress increases from 10 kPa to 40 kPa as shown in Figure 7(a).

The permanent strain develops in the first 100 cycles under the effective confining pressure of 20 kPa accounts for 36.8%, 53.5%, and 53.7% of the total permanent strain under three cyclic deviator stresses of 10 kPa, 25 kPa, and 40 kPa, respectively as shown in Figure 7(a). However, these corresponding values are 24.7%, 32.7%, and 43.8% and 18.1%, 33.9%, and 36.1% for the effective confining pressure are 50 kPa and 100 kPa, respectively as shown in Figures 7(a) and 6(b). This difference indicates that under a small effective confining pressure, permanent strain accumulates more than that under a high effective confining pressure in the beginning cycles, which is also called the conditioning period.

Several sudden upward rises occur on the curves at the cycle number of around 100000, especially for D_20_40, as shown in Figure 7(a). This phenomenon might be owing to the sudden sliding or even crushing happened in the specimen. As shown in Figures 7(b) and 7(c), the

developments of permanent axial strain rise more gradually. As listed in Table 2, it is noted that the value of $\Delta q_{cyc} / \Delta q_{sta,f}$ is 0.244 for D_20_40, which is obviously higher than those of other eight specimens. This indicates that a specimen with a higher $\Delta q_{cyc} / \Delta q_{sta,f}$ value is more prone to reach an unstable state and gains a sudden increase in the permanent axial strain.

It should be emphasized that the strain accumulated in cycle No.1 be significant for every specimen, which is probably due to the sudden compaction on the initially slacking structure of the specimen. Therefore, to better describe the developing trend of the permanent axial strain, the development is divided into two parts according to cycle number: the strain in cycle No.1 and the strain in the following cycle. The total permanent axial strain is expressed as:

$$\Delta\varepsilon_{ap} = \Delta\varepsilon_{ap,1} + \Delta\varepsilon_{ap,N} \tag{1}$$

For the strain happened in the first cycle ( $\Delta\varepsilon_{ap,1}$ ), it has a linear relationship with $\Delta q_{cyc} / \Delta q_{sta,f}$ , as shown in Figure 8. The best fitting linear relationship is expressed as:

$$\Delta\varepsilon_{ap,1} = k \cdot \frac{\Delta q_{cyc}}{\Delta q_{sta,f}} \tag{2}$$

where *k* is the slope of the fitting linear line, and is 0.2055 for this case. With a correlation coefficient ($R^2$) of 0.9452, this equation is accurate enough to predict the strain occurred in the first cycle.

Regarding the permanent axial strain $\Delta\varepsilon_{ap.N}$ after cycle 1, $\Delta\varepsilon_{ap.N}$ keeps accumulating at a diminishing rate with the increase of cycle number. The limited cycle number in a cyclic triaxial test cannot simulate the real long-term deformation behavior in the field where the subgrade may experience around millions of cycles of loading per year with a service life of possibly 100 years. Therefore, a well-known log-hyperbolic function first proposed by Yin (1999), is adopted here to

describe the development trend of accumulated permanent strain with $N$ and extrapolation to the final limit permanent strain when $N$ goes to infinity by using the known test data. The function is expressed as:

$$\Delta\varepsilon_{ap,N} = \frac{\log(\frac{N-1+N_0}{N_0})}{a+b\cdot\log(\frac{N-1+N_0}{N_0})} \quad (N \geq 1) \tag{3}$$

where $\Delta\varepsilon_{ap,N}$ is the permanent axial strain accumulated during cycle 2 to cycle $N$. In fact, Equation (3) is an extended hyperbolic function when taking $\log(\frac{N-1+N_0}{N_0})$ as a variable. $N_0$, a, and b are three constant parameters with clear physical meanings. It is deduced that the limit value of $\Delta\varepsilon_{ap.N}$ is equal to $1/b$ when the cyclic number $N$ rises to infinity. Therefore, parameter $b$ is regarded as the reciprocal of the accumulated permanent axial strain limit, denoted as $\Delta\varepsilon_{ap.\infty}$. If there is no limit, that is, $\Delta\varepsilon_{ap.\infty}$ is infinite, then $1/b = \infty$. If $1/b = \infty$, Equation (3) can be expressed as:

$$\Delta\varepsilon_{ap,N} = \frac{1}{a}\log(\frac{N-1+N_0}{N_0}) \ (\text{for } \frac{1}{b} = \infty) \tag{3a}$$

It can be seen that value of $1/a$ is the slope of the $\Delta\varepsilon_{ap,N}$ and $\log(\frac{N-1+N_0}{N_0})$. The parameter of $N_0$ is closely related to the initial rate of the accumulated permanent axial strain, which is expressed as:

$$\dot{\varepsilon}_{ap,N}\big|_{N=1} = \frac{1}{\ln(10)}\cdot\frac{1}{a\cdot(N_0+N-1)}\Big|_{N=1} = \frac{1}{aN_0\ln(10)} \tag{3b}$$

It can be seen that the ratio of $\frac{1}{aN_0\ln(10)}$ defines the initial accumulated permanent axial strain rate at the first cycle number.

As suggested by Yin (1999), $N_0$ should be chosen in advance. In this study, to balance the performance of the prediction model and establishing an easy-to-use bridge between static and cyclic tests, $N_0$ is chosen as 1000. Equation (3) can be written as:

$$\frac{\log(\frac{N-1+N_0}{N_0})}{\Delta\varepsilon_{ap,N}} = a + b \cdot \log(\frac{N-1+N_0}{N_0}) \quad (N \geq 1) \tag{4}$$

Equation (4) has been used to fit all data linearly in the plot of $\log((N-1+N_0)/N_0)$ and $\log((N-1+N_0)/N_0)/\Delta\varepsilon_{ap,N}$ from 9 cyclic tests to that values of *a* and *b* are determined. As an example, the original data of specimen D_20_40 and the fitting straight line are presented in Figure 9. The interception of the fitting straight line and the $\log((N-1+N_0)/N_0)/\Delta\varepsilon_{ap,N}$ - axis and the slope are a and b, respectively. Likewise, 9 sets of best-fit *a* and *b* for 9 specimens are listed in Table 3 as "best-fit" to data from each test. Examining the best-fit *a* and *b*, it is found that there are one linear relationship between *a* and $1/(\Delta q_{cyc}/\Delta q_{sta,f})$, and another linear relationship between 1/*b* and $\Delta q_{cyc}/\Delta q_{sta,f}$, as shown in Figure 10. These two linear relationships are expressed as follows:

$$a = 0.4959/(\Delta q_{cyc}/\Delta q_{sta,f}) + 1.209 \tag{5}$$

$$1/b = \Delta\varepsilon_{ap,N,L} = 0.3475(\Delta q_{cyc}/\Delta q_{sta,f}) + 0.071 \tag{6}$$

In this way, the values of both *a* and *b* values are related to the stress ratio $\Delta q_{cyc}/\Delta q_{sta,f}$. The values of all calculated *a* and *b* values as "predicted" based on Equation (5) and Equation (6) are also listed in Table 3. It is noted that Equation (5) and Equation (6) are from the best-fitting of data from all 9 tests.

Once the values of $a$ and $b$ are known plus the predetermined $N_0$ and $\Delta\varepsilon_{ap,1}$, the predicted equation for the permanent axial strain is established as:

$$\begin{cases} \Delta\varepsilon_{ap,1} = k \cdot \dfrac{\Delta q_{cyc}}{\Delta q_{sta,f}} \\ \Delta\varepsilon_{ap,N} = \dfrac{\log(\dfrac{N-1+N_0}{N_0})}{a + b \cdot \log(\dfrac{N-1+N_0}{N_0})} \end{cases} \tag{7a}$$

Subtituting Equation (7a), (5) and (6) into Equation (1) to obtain the final total permanent axial strain $\Delta\varepsilon_{ap}$ under any cycle number $N$ ($N \geq 1$) for this case, as expressed:

$$\Delta\varepsilon_{ap,N} = 0.2055 \times \frac{\Delta q_{cyc}}{\Delta q_{sta,f}} + \frac{\log(\dfrac{N-1+N_0}{N_0})}{0.4959 \Big/ (\dfrac{\Delta q_{cyc}}{\Delta q_{sta,f}}) + 1.209 + \left(0.3475(\dfrac{\Delta q_{cyc}}{\Delta q_{sta,f}}) + 0.071\right) \cdot \log(\dfrac{N-1+N_0}{N_0})} \tag{7b}$$

where $N_0$ is 1000.

Figure 11 shows the plots of permanent axial strain versus log($N$) ($N$=cycle number) for 9 tests and the predicted curves, which are based on Equation (7b). The predicted curves are in good agreement with the test data. With the static test result and the expected cyclic stress level, the final limit value and the accumulated permanent axial strain with cycle number could be easily predicted. The proposed Equation (7b) is accurate enough to describe the accumulated permanent axial strains of the subgrade under the small cyclic stress levels, which are the normal cases for HSR.

The relationships between the development of volumetric strain and the accumulation of axial strain are shown in Figure 12. Under the same effective confining pressure of 20 kPa, three

specimens firstly exhibit contraction and then dilation. Both of the volume contraction extent and the permanent axial strain at phase transfer point increase with the growth of cyclic deviator stress. The behaviors of specimens under other two effective confining pressures differ greatly. Even though both D_50_10 and D_100_10 show the similar phase transfer from contraction to dilation, the rest four specimens only exhibit contraction. It is noted that the volumetric strain gradually increases although no obvious variation happens in the permanent axial strain. Based on the results, it is recommended that the engineers not only focus on the monitoring or controlling of the vertical deformation of subgrade but also pay attention to the effect of the lateral deformation. If the excessive lateral deformation happens, the level of confining pressure may be weakened so that excessive volumetric strains develop further, even lead to failure of the subgrade.

***Resilient Behavior of the Fill in Cyclic Compression Tests***

Resilient modulus is defined as the ratio ($\Delta q_{cyc} / \Delta \varepsilon_{cyc}^{e}$) of the amplitude of cyclic deviator stress, $\Delta q_{cyc}$, and the recoverable strain, $\Delta \varepsilon_{cyc}^{e}$, in every loading cycle. Figure 13 shows the variation of resilient modulus with peak cyclic deviator stress. The peak cyclic deviator stress, $q_{cyc,p}$, is defined shown in Figure 3. It is found that the resilient modulus decreases slightly with the increase of $p^{'}$ and $q_{cyc,p}$ when $q_{cyc,p}$ is less than 150 kPa. However, the resilient modulus is increased with $q_{cyc,p}$ obviously when $q_{cyc,p}$ is above 150 kPa. The particle movement can explain this phenomenon in a micro perspective. Firstly, numerous fine particles surrounded the large particles in the soil specimens so that the deformation of the specimen was mainly controlled by the behavior of the fine particles when the stress level was low. The low sliding resistance of fine particles and the lubricant effect of water facilitate the deformation of the tested specimen.

348 Secondly, the slight variation in the stress condition was majorly sustained by the soil skeleton of
349 big particles so that the behavior of fine particles had no obvious change when the peak cyclic
350 deviator stress was increased from 0 to 150 kPa. Under a higher stress level, the effect of the
351 behavior of big particles prevailed over the fine particles, and this advantage became more obvious
352 when the stress level was increased due to the strengthening of the interlocking and the sliding
353 resistance between big particles.

354 The well-known Uzan model (Uzan 1985) is expressed as follows:

355 $$M_r = k_3 p_0 (\frac{\theta}{p_0})^{k4} (\frac{q}{p_0})^{k5} \quad (8)$$

356 where $\theta$ is bulk stress, $p_0$ is the atmospheric pressure (100 kPa), $q$ is the deviator stress and the $k_1$,
357 $k_2$, $k_3$, $k_4$, and $k_5$ are the regression parameters. Equation (8) is used to describe the trend of the $M_r$
358 values when the $q_{cyc,p}$ surpasses 150 kPa. Using regression analysis, the best-fit $k_3$, $k_4$, and $k_5$ are
359 0.149, 0.428, and 0.906, respectively. Then the predicted surface using Equation (8) is depicted in
360 Figure 13. It can be observed that this model may underestimate the resilient modulus if the peak
361 cyclic deviator stress is small, which was also reported by Yau and Von (2002). A particular
362 concern should, therefore, be given to the resilient modulus, because of the low-stress condition
363 and possible high fine content in the subgrade of HSR. The present study only illustrates the
364 unconformity between the existing models and testing data. Further studies are recommended on
365 the effect of different levels of fine contents and water contents to ascertain the underlying reasons.
366

367 **CONCLUSIONS**

368 In this study, static and cyclic compression tests were performed on the scaled-down
369 subgrade fill of HSR with aims to examine the accumulated permanent axial strain development
370 and the resilient behavior under the low-stress condition. The main observations and findings from

this study are as follows:

(a) The data from static compression tests suggests that the stress-strain-strength behavior is largely influenced by the effective confining pressure. For the specimens consolidated under the effective confining pressures of 20 and 50 kPa, the stress-strain behavior showed strain softening. However, the stress-strain behavior showed strain hardening for the specimens when the effective confining pressure was 100 kPa. The *q/p'* ratio moved toward nearly a constant value around 2 with the increase of axial strain. All the specimens exhibited shear dilation phenomenon, which was more evident when the effective confining pressure was smaller.

(b) The results from the cyclic tests show that the permanent axial strain could be aggravated by higher cyclic deviator stress, while, greatly mitigated by the higher effective confining pressure. The specimens, which are subjected to the $\Delta q_{cyc}$ of 25 kPa or 40 kPa, transfer from dilation to contraction under the cyclic loading with the increase of the effective confining pressure. However, for those cases with a relatively small $\Delta q_{cyc}$ of 10 kPa, the specimens keep dilating under the cyclic loading irrespective of the change in effective confining pressure.

(c) A new empirical equation is proposed to predict the accumulated permanent axial strain with cycle number and the $\Delta q_{cyc} / \Delta q_{sta,f}$ . Furthermore, a method for determining all parameters used in this equation is described elaborately. The performance of this equation is evaluated by comparing the results obtained from the prediction and experimental data. It is found that the predicted accumulated permanent axial strain with cycle number is in good agreement with test data.

(d) It is found that when the peak cyclic deviator stress is smaller than 150 kPa, the resilient

modulus decreases slightly with the increase of stresses, which raises difficulties in adopting the widely-used model.

## ACKNOWLEDGEMENT

The work in this paper is supported by a Key Project Grant (Grant No. U1234204) from National Natural Science Foundation of China *via* PolyU Shenzhen Research Institute, and The Hong Kong Polytechnic University, China.

## REFERENCES

AASHTO. (2007). "Standard method of test for determining the resilient modulus of soils and aggregate material." *AASHTO T307,* Washington. D.C. VA.

Baldi, G., and Nova, R. (1984). "Membrane penetration effects in triaxial testing." *J. of Geotech. Engrg*. 110 (3), 403-420.

Barksdale, R. D., and Itani, S. Y. (1989). "Influence of aggregate shape on base behaviour." *Trans. Res. Rec.* Washington, D.C., 1227, 173-182.

British Standards Institute. (1990). "Methods of test for soils for civil engineering purposes." *BS 1377*, London, England.

Chen R.P., Zhou W.H., and Chen Y.M. (2009). "Influences of Soil Consolidation and Pile Load on the Development of Negative Skin Friction of a Pile." *Comput. Geotech*. 36(8), 1265-1271.

Guo, J. H. (2012). "Study on dynamic response of granular type A and type B fillings of high speed railway." *Soil Engrg. and Found.*, 26(10), 116-120. (in Chinese)

Hicks, R. G., and Monismith, C. L. (1971). "Factors influencing the resilient properties of granular materials." *High. Res. Re*. Washington, D. C., 345, 15-31.

Indraratna, B, Lackenby, J and Christie, D. (2005). "Effect of confining pressure on the degradation of ballast under cyclic loading." *Géotechnique,* 55 (4), 325-328.

Jiang, Y., Han, J., and Zheng, G. (2014). "Numerical Analysis of a Pile -Slab-Supported Railway Embankment." *Acta Geotech.,* 9 (3), 499-511.

Lackenby, J., Indraratna, B., McDowell, G., and Christie, D. (2007). "Effect of confining pressure on ballast degradation and deformation under cyclic triaxial loading." *Géotechnique,* 57 (6), 527-536.

Lekarp, F. (1997). "Permanent deformation behavior of unbound granular materials." Licentiate thesis, Royal Institute of Technology, Stockholm.

Lekarp, F., and Dawson, A. (1998). "Modelling permanent deformation behaviour of unbond granular materials." *Constr.and Build. Mater.,* 12 (1), 9-18.

Marre, J. H. (1982). "Aspects of the design and behaviour of road pavements with granular material base layers." Ph.D. thesis, Univ. of Pretoria, Pretoria, South Africa (in Afrikaans).

Ministry of Railway, (2009). "Code for Design of High Speed Railway." *TB 10020,* Beijing, China.

Monisimith, C. L., Seed, H. B., Mitry, F. G., and Chan, C. K. (1967). "Prediction of pavement deflections from laboratory tests." *Proc. of 2nd Int. Conf. of Str. Des. of Asph. Pav*. July, Michigan, 109-140.

Qu, C. Z., Wang, Y. H., Wei, L. M. and Guo, Z. G. (2012). "In-situ test and analysis of vibration of subgrade for Wuhan-Guangzhou High-Speed Railway." *Rock and Soil Mech.,* 33 (5), 1451-1461 (in Chinese).

438 Raymond, G. P., and Williams, D. R. (1978). "Repeated load triaxial tests on a dolomite ballast."
439 *J. of Geotech. Engrg. Div.*, ASCE, 104(7), 1013-1029.
440 Seed, H. B., Mitry. F. G., Monismith, C. L., and Chan, C. K. (1967). "Prediction of flexible
441 pavement deflections from laboratory repeated load tests." *NCHRP Rep. No. 35*, National
442 Cooperative Highway Research Program.
443 Sweere, G. T. H. (1990). "Unbound granular bases for roads." Ph.D. Thesis, Univ. of Delft, Delft,
444 Netherlands.
445 Thakur, P. K., Vinod, J. S., and Indraratna, B. (2013) "Effect of confining pressure and frequency
446 on the deformation of ballast." *Géotechnique*, 63 (9), 786-790.
447 Thom, N. H. (1988), "Design of road Foundation." Ph.D thesis, Univ. of Nottingham, Nottingham,
448 England.
449 Uzan, J. (1985). "Characterization of granular material." *Trans. Res. Rec.* Washington, D.C., *1022*,
450 52-59.
451 Vallerga, B. A., Seed, H. B., Monismith, C. L., and Cooper, R. S. (1975). "Effect of shape, size
452 and surface roughness of aggregate particles on the strength of granular materials." *Road and*
453 *Pav. Mater.*, ASTM, Special Technical Publication, 212, 63-76.
454 Wolff, H. (1992). "The elasto-plastic behaviour of granular pavement layers in South Africa."
455 Ph.D. thesis, Univ. of Pretoria, Pretoria, South Africa.
456 Yau, A., and Von Quintus, H. L. (2002). "Study of LTPP laboratory resilient modulus test data
457 and response characteristics: final report." *Federal Highway Administration*, Publication No.
458 FHWA-RD-02-051.
459 Ye, Y. S. (2004). "Discussion on the Classification of Railway Subgrade Fills." *China Railway*
460 *Science*, 25 (2), 35-40. (In Chinese)

461 Yideti, T. F., Birgisson, B., Jelagin, D., and Guarin, A. (2013). "Packing theory-based framework
462 to evaluate permanent deformation of unbound granular materials." *Int. J. of Pavement*
463 *Engrg.*, 14 (3), 309-320.
464 Yin, J. H. (1999). "Non-linear creep of soils in oedometer tests." *Géotechnique*, 49(5), 699-707.
465 Zhao, L. S., Zhou W. H., Fatahi, B., Li, X. B., and Yuen, K.-V. (2016) "A Dual Beam Model for
466 Geosynthetic-Reinforced Granular Fill on an Elastic Foundation." *Appl. Math. Model.*, 40
467 (21-22), 9254-9268.

**Table 1. Basic characteristics of tested soils**

| Basic characteristics | Value |
|---|---|
| Coefficient of uniformity ($C_u$) | 1303.6 |
| Coefficient of curvature ($C_c$) | 384.89 |
| Content of fines (particles of d < 0.075 mm) (%) | 15.3 |
| Specific gravity ($G_s$) | 2.73 |
| Maximum void ratio ($e_{max}$) | 0.78 |
| Minimum void ratio ($e_{min}$) | 0.25 |
| Maximum dry density ($\rho_{max,dry}$, kg/m$^3$) | 2195.5 |
| Plastic limit for particles of d < 0.075 mm (%) | 22 |
| Liquid limit for particles of d < 0.075 mm (%) | 40 |

**Table 2. The testing scheme**

| Test name | $\sigma_3'$ (kPa) | $\Delta q_{cyc}$ (kPa) | $\Delta q_{cyc} / \Delta q_{sta,f}$ | Cycle number | $\sigma_1'/\sigma_3'$ (stress ratio for consolidation) |
|---|---|---|---|---|---|
| S_20 | 20 | - | - | - | 2 |
| S_50 | 50 | | | | |
| S_100 | 100 | | | | |
| D_20_10 | 20 | 10 | 0.061 | $5\times10^5$ | |
| D_20_25 | | 25 | 0.153 | | |
| D_20_40 | | 40 | 0.244 | | |
| D_50_10 | 50 | 10 | 0.040 | | |
| D_50_25 | | 25 | 0.099 | | |
| D_50_40 | | 40 | 0.159 | | |
| D_100_10 | 100 | 10 | 0.019 | | |
| D_100_25 | | 25 | 0.048 | | |
| D_100_40 | | 40 | 0.076 | | |
| RM_Sat | 20, 50, 75, 100, 150, 200 | 10, 20, 30, 50, 70, 100 | - | 100 for each step | 1, 1.25, 1.5, 2 |

**Table 3. The values of the parameters in Equation (3) and (4) by curve fitting and prediction**

| | $\frac{\Delta q_{cyc}}{\Delta q_{sta,f}}$ | a (best- fit) | b (best- fit) | a (predicted) | b (predicted) | 1/b (limit of $\Delta\varepsilon_{ap,N}$, $N \geq 1$, predicted) |
|---|---|---|---|---|---|---|
| D_20_10 | 0.061 | 9.323 | 8.429 | 8.359 | 10.84 | 0.092 |
| D_20_25 | 0.153 | 5.694 | 9.002 | 3.779 | 8.058 | 0.124 |
| D_20_40 | 0.244 | 2.387 | 6.020 | 2.442 | 6.412 | 0.156 |
| D_50_10 | 0.040 | 14.74 | 12.46 | 11.65 | 11.79 | 0.085 |
| D_50_25 | 0.099 | 11.23 | 9.756 | 5.551 | 9.475 | 0.106 |
| D_50_40 | 0.159 | 2.947 | 8.394 | 3.644 | 7.920 | 0.126 |
| D_100_10 | 0.019 | 27.18 | 11.99 | 18.81 | 12.88 | 0.078 |
| D_100_25 | 0.048 | 10.95 | 14.40 | 10.16 | 11.42 | 0.088 |
| D_100_40 | 0.076 | 3.294 | 9.876 | 6.963 | 10.26 | 0.098 |

Figure 1

Click here to download Figure Figure 1.tif

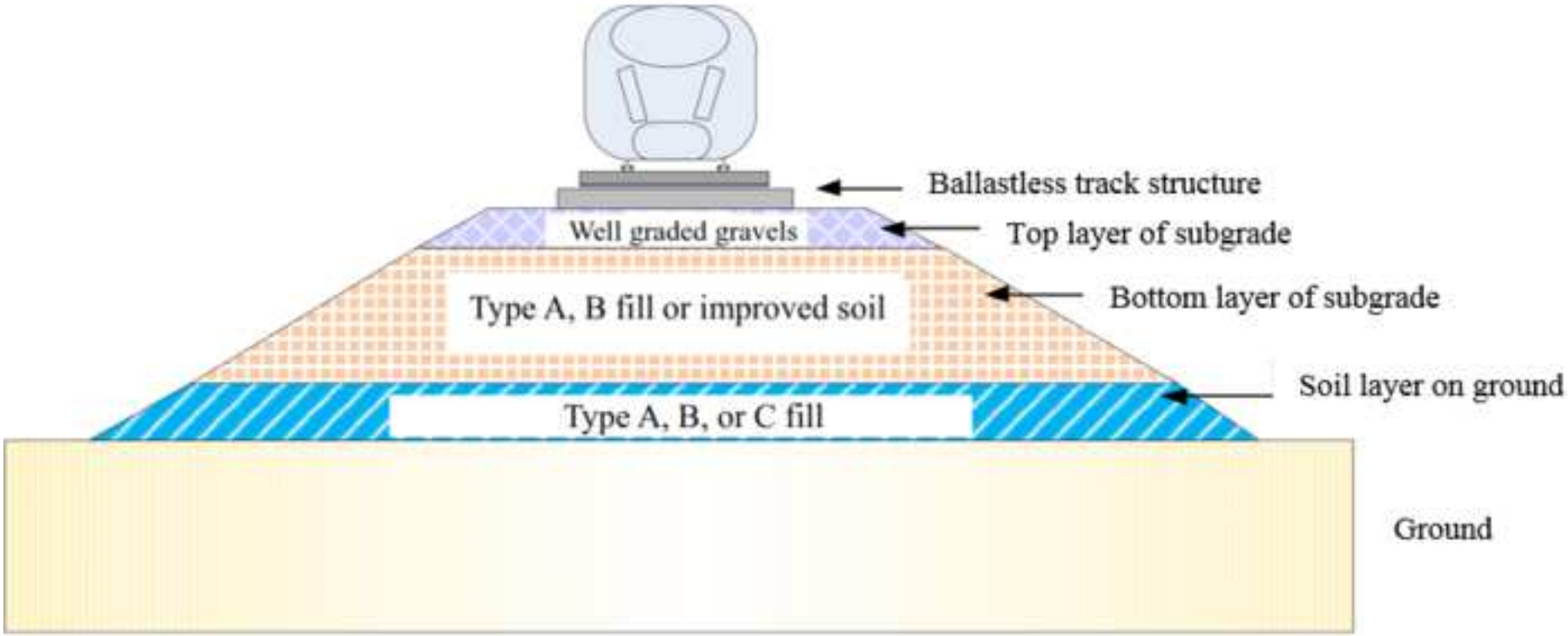

Figure 2

Click here to download Figure Figure 2.tif

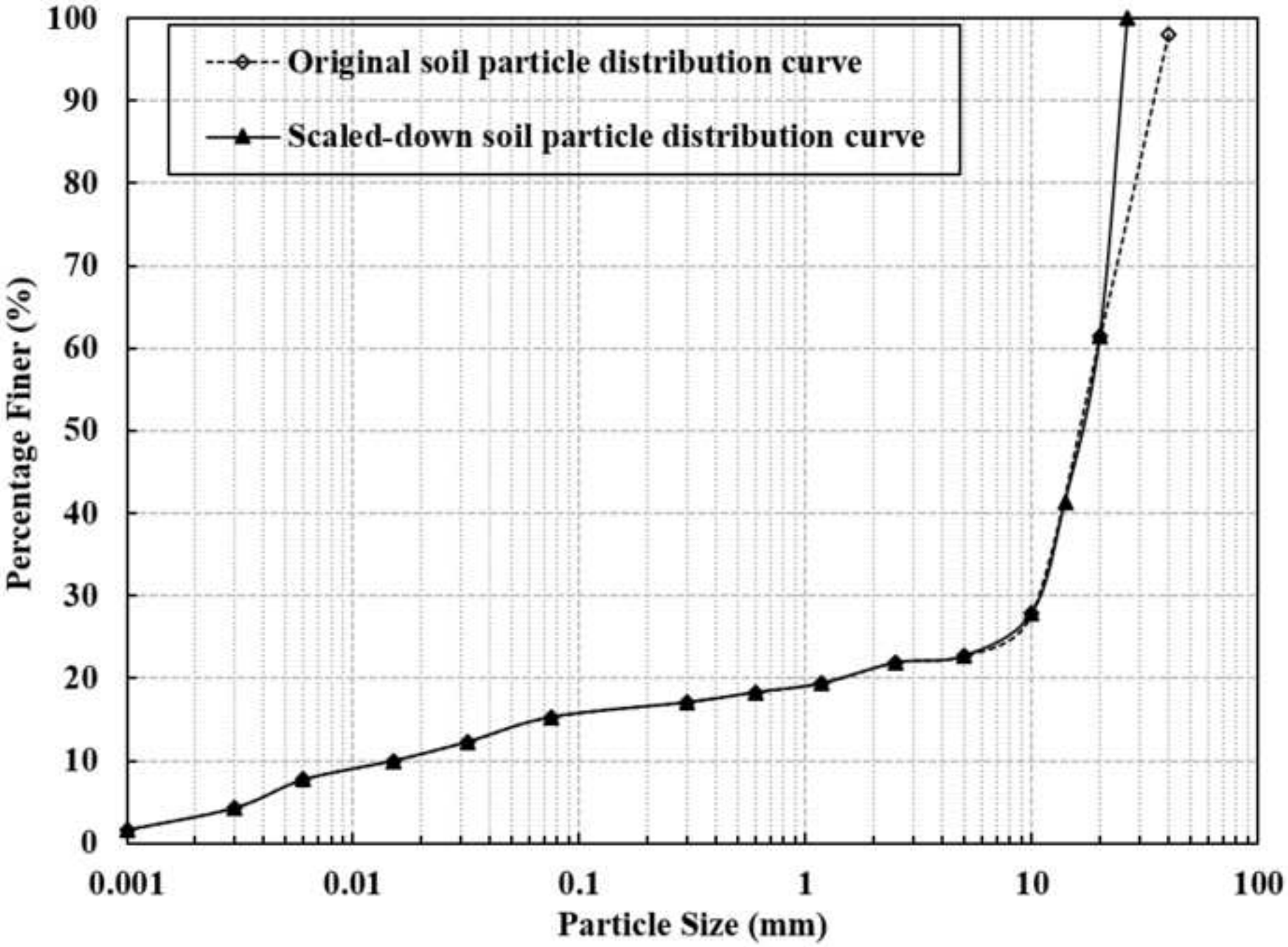

Figure 4

Click here to download Figure Figure 4.tif

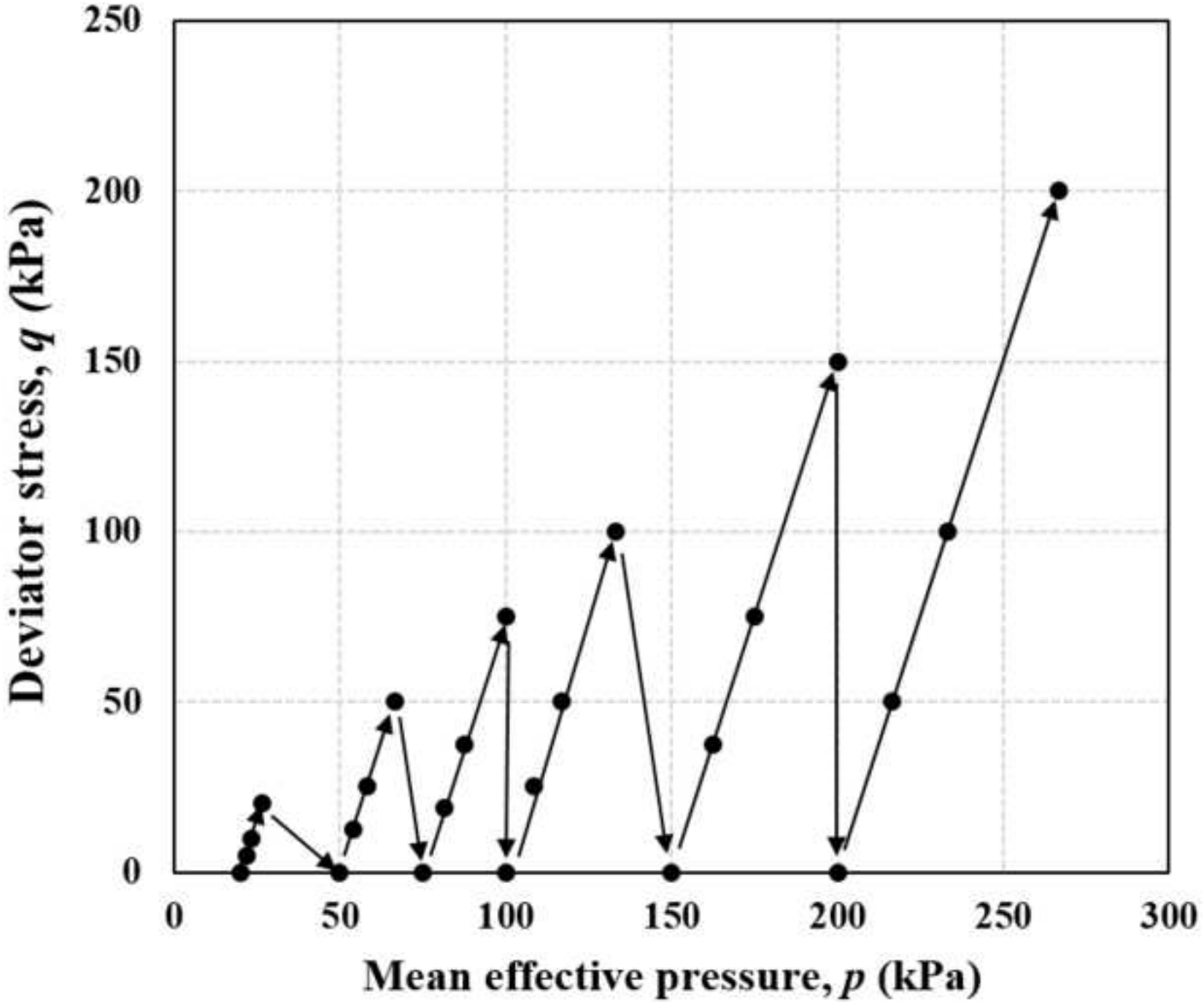

Figure 5

Click here to download Figure Figure 5.tif

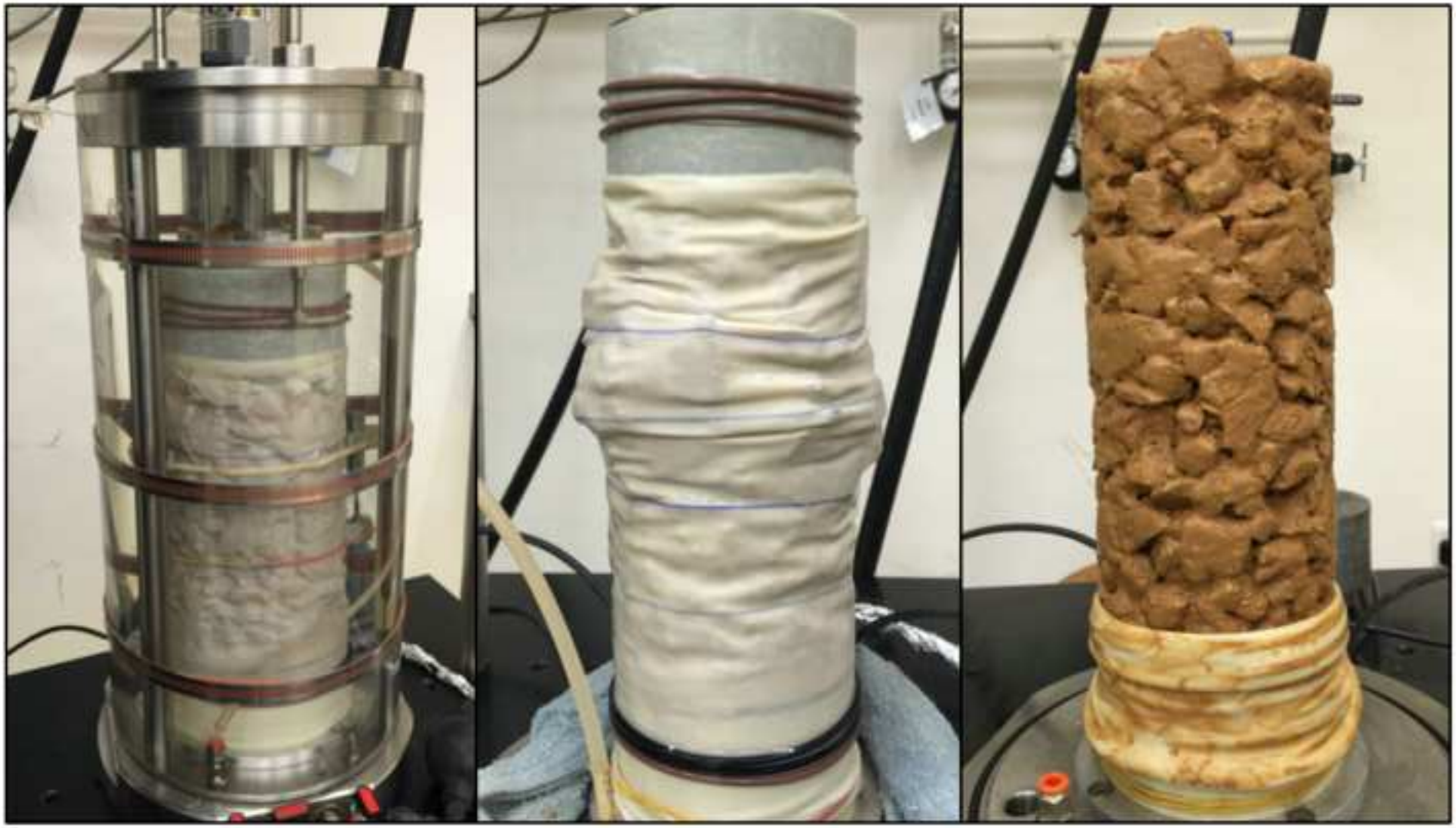

(a) (b) (c)

Figure 3

Click here to download Figure Figure 3.tif

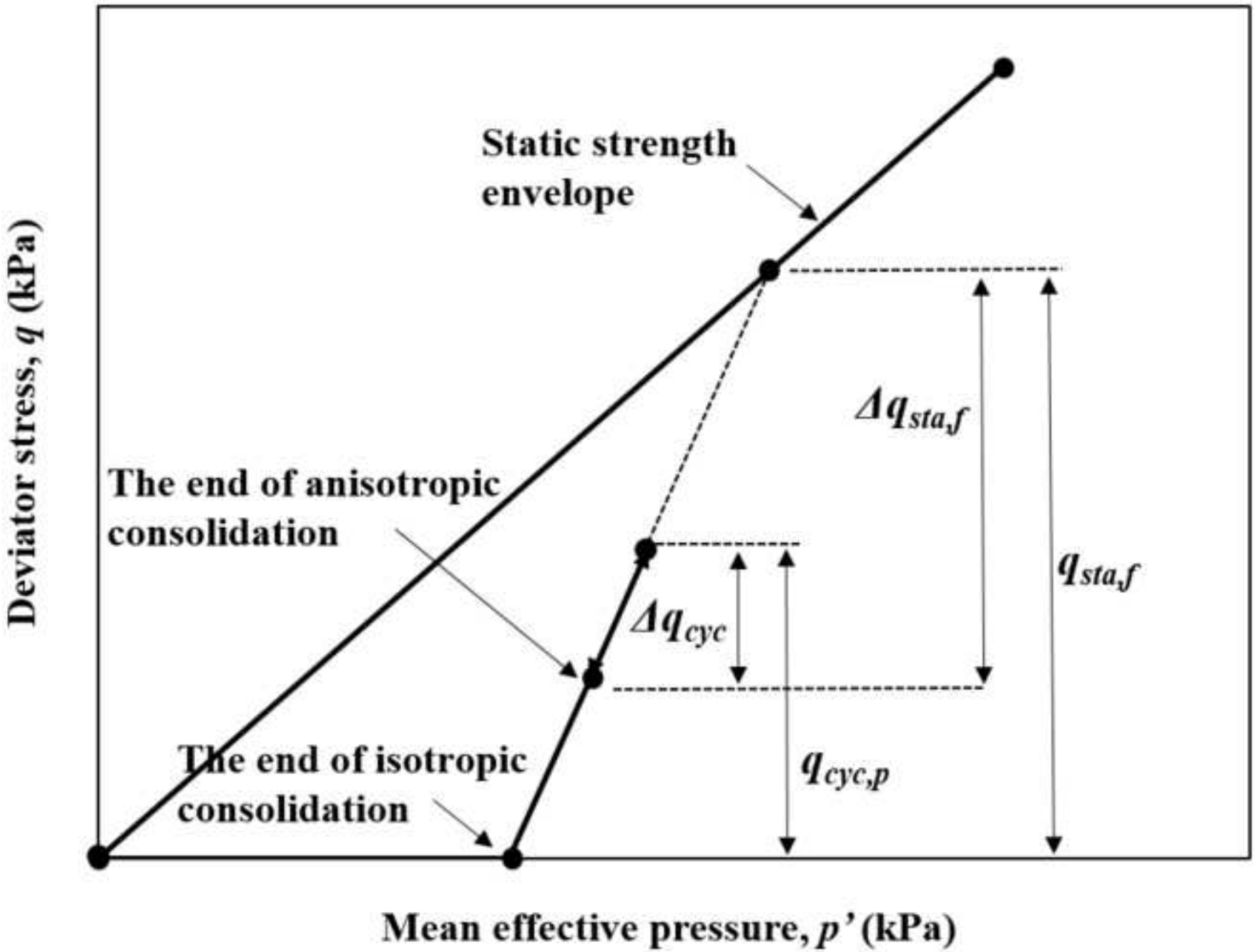

Figure 6 (a)

Click here to download Figure Figure 6 (a).tif

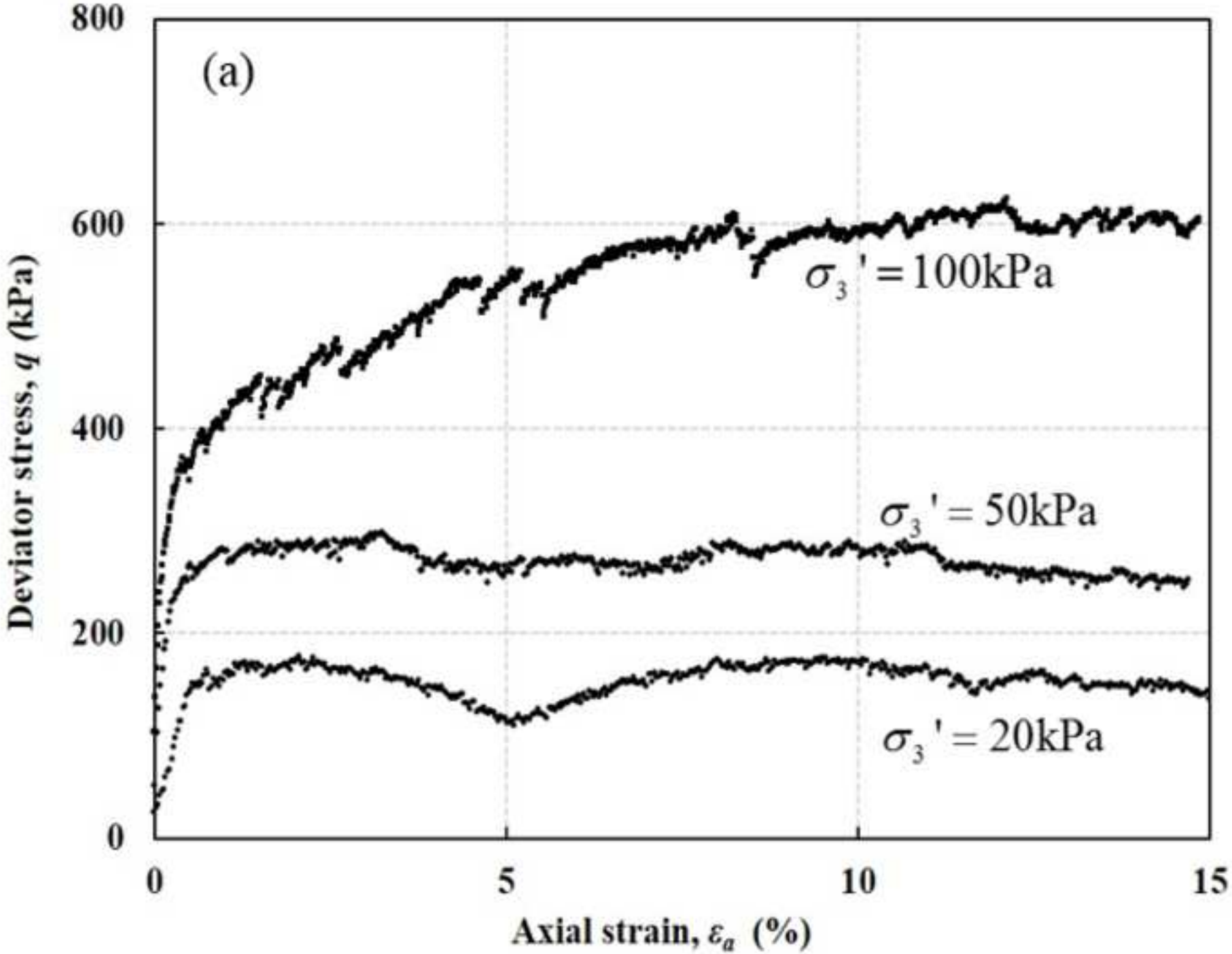

Figure 6 (b)

Click here to download Figure Figure 6 (b).tif

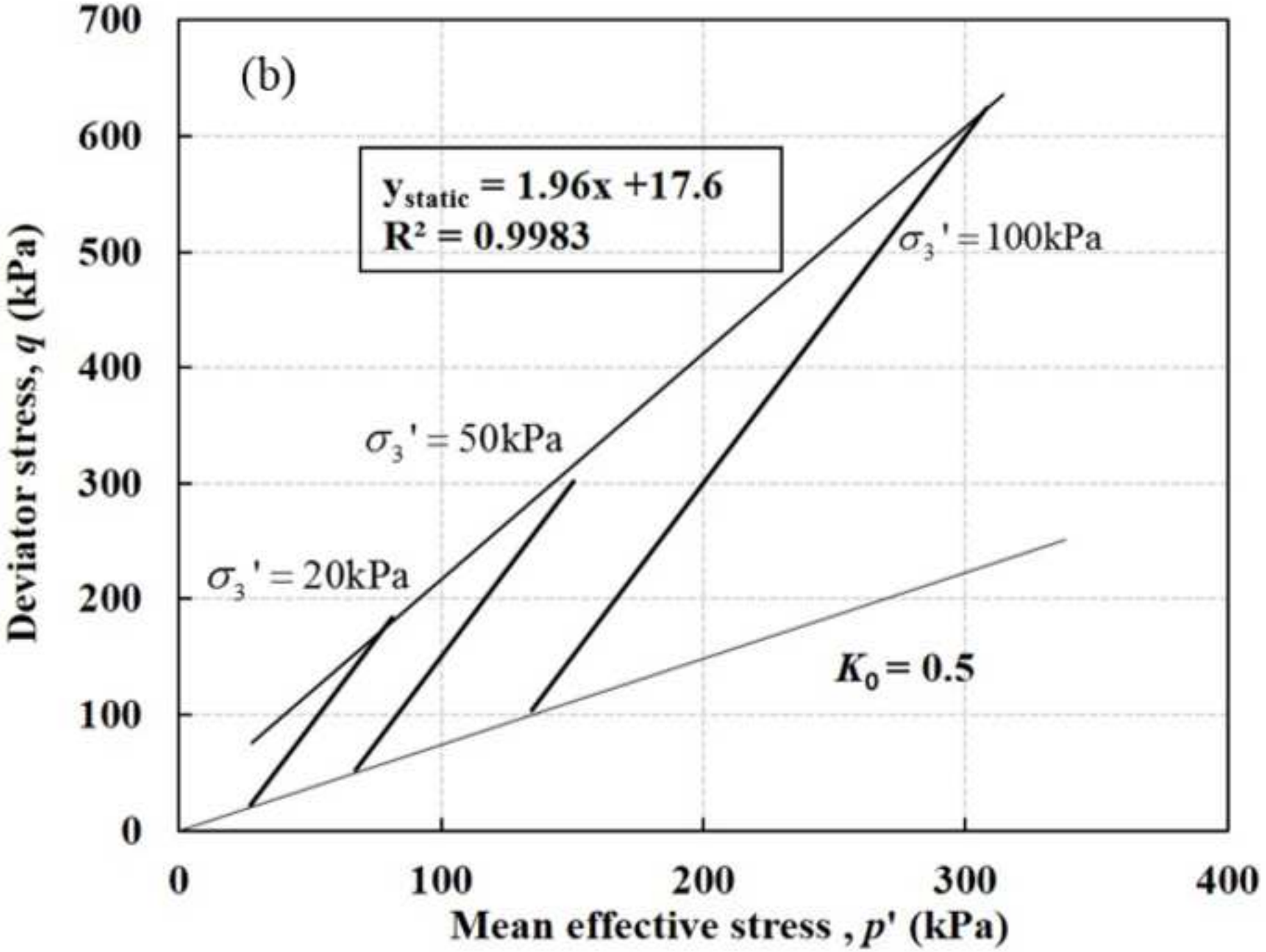

Figure 6 (c)

Click here to download Figure Figure 6 (c).tif

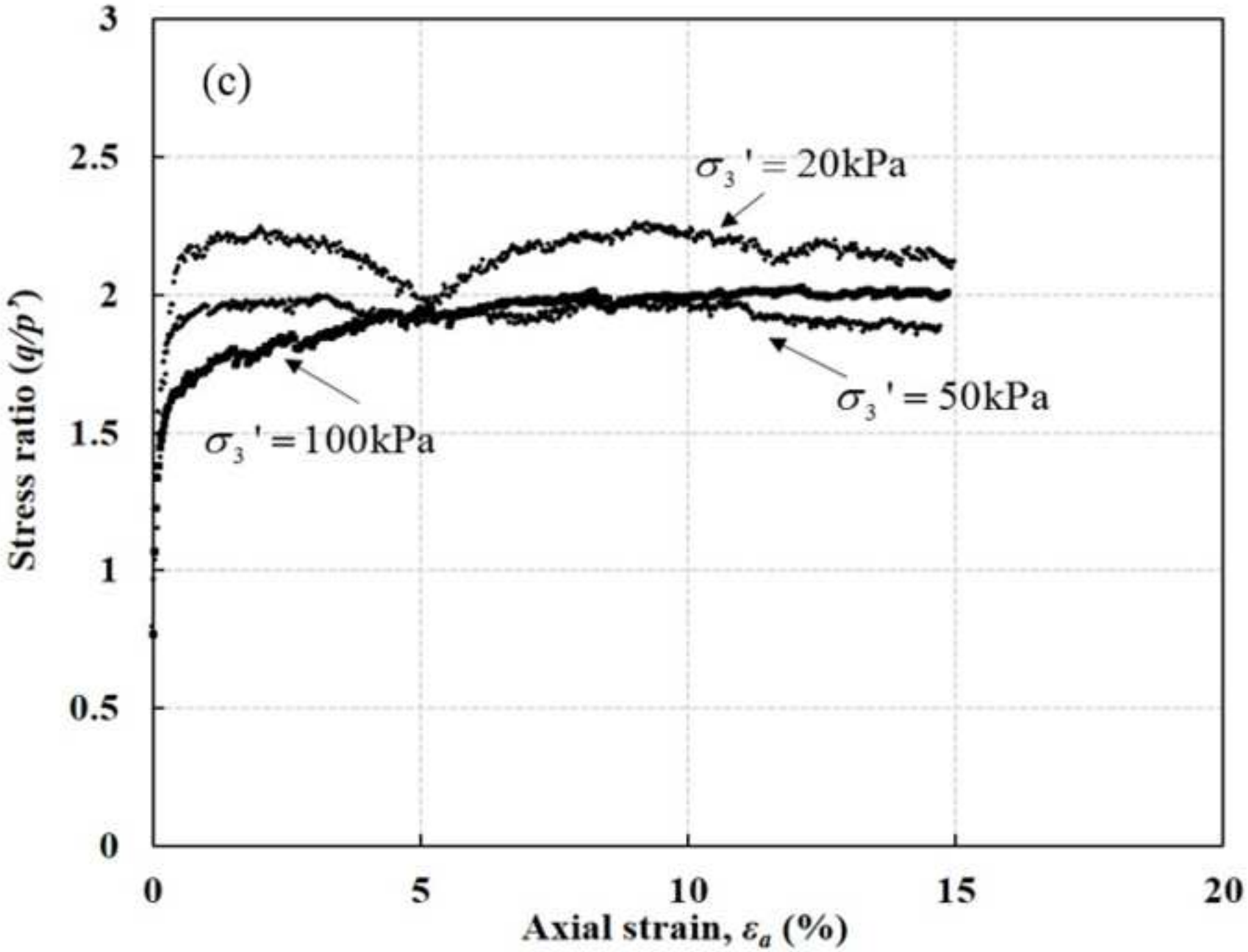

Figure 7 (a)

Click here to download Figure Figure 7 (a).tif

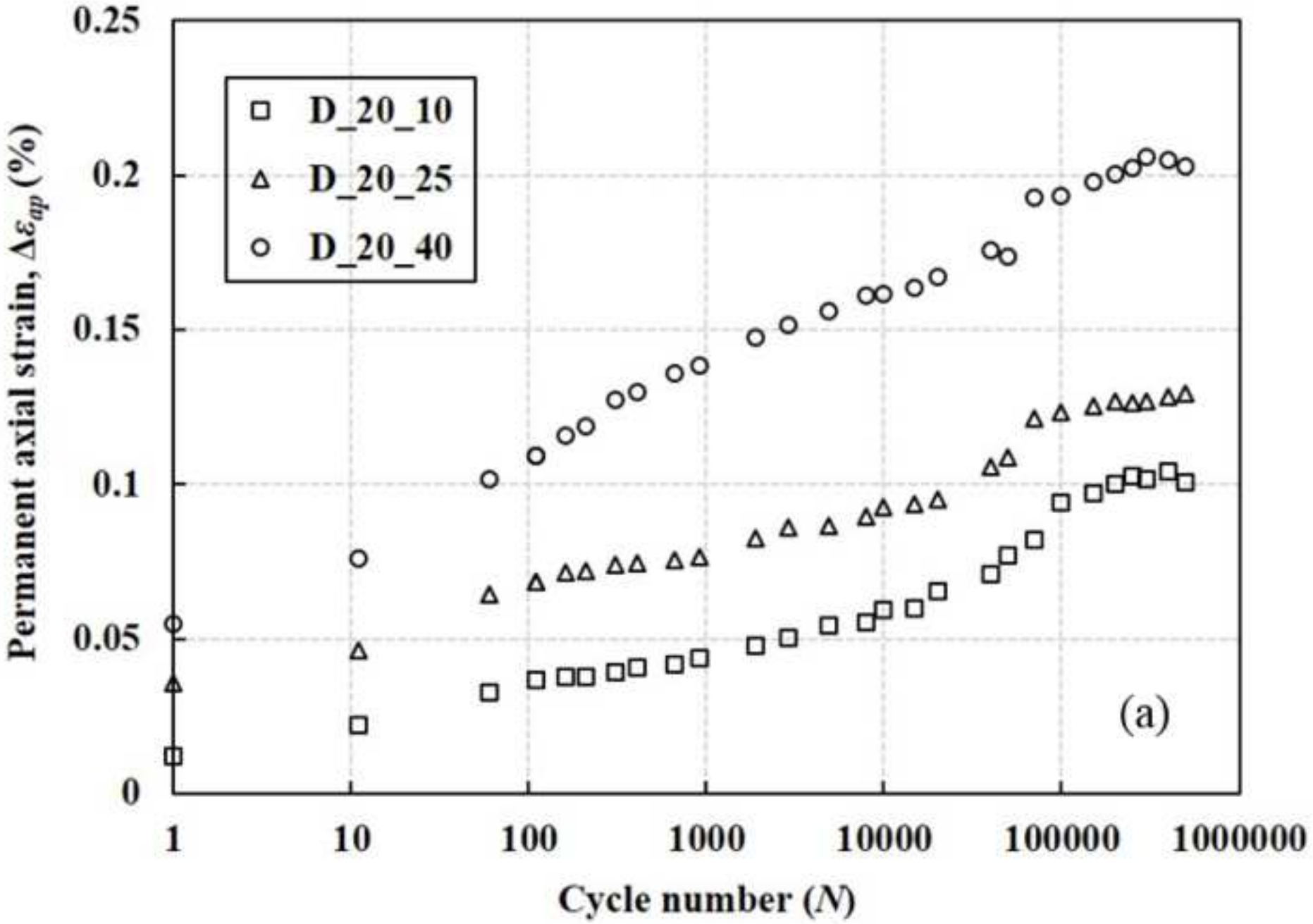

Figure 7 (b)

Click here to download Figure Figure 7 (b).tif

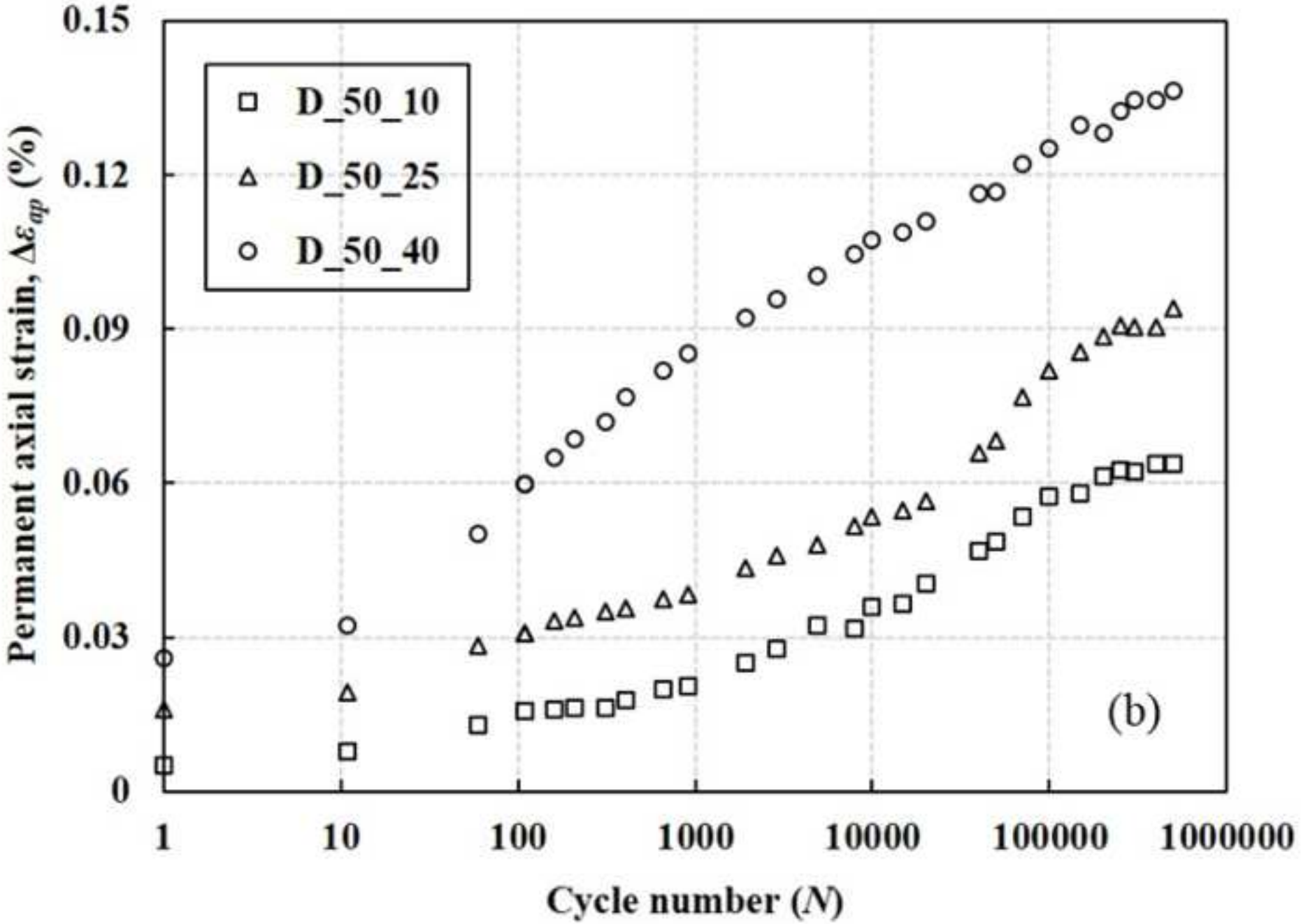

Figure 7 (c)

Click here to download Figure Figure 7 (c).tif

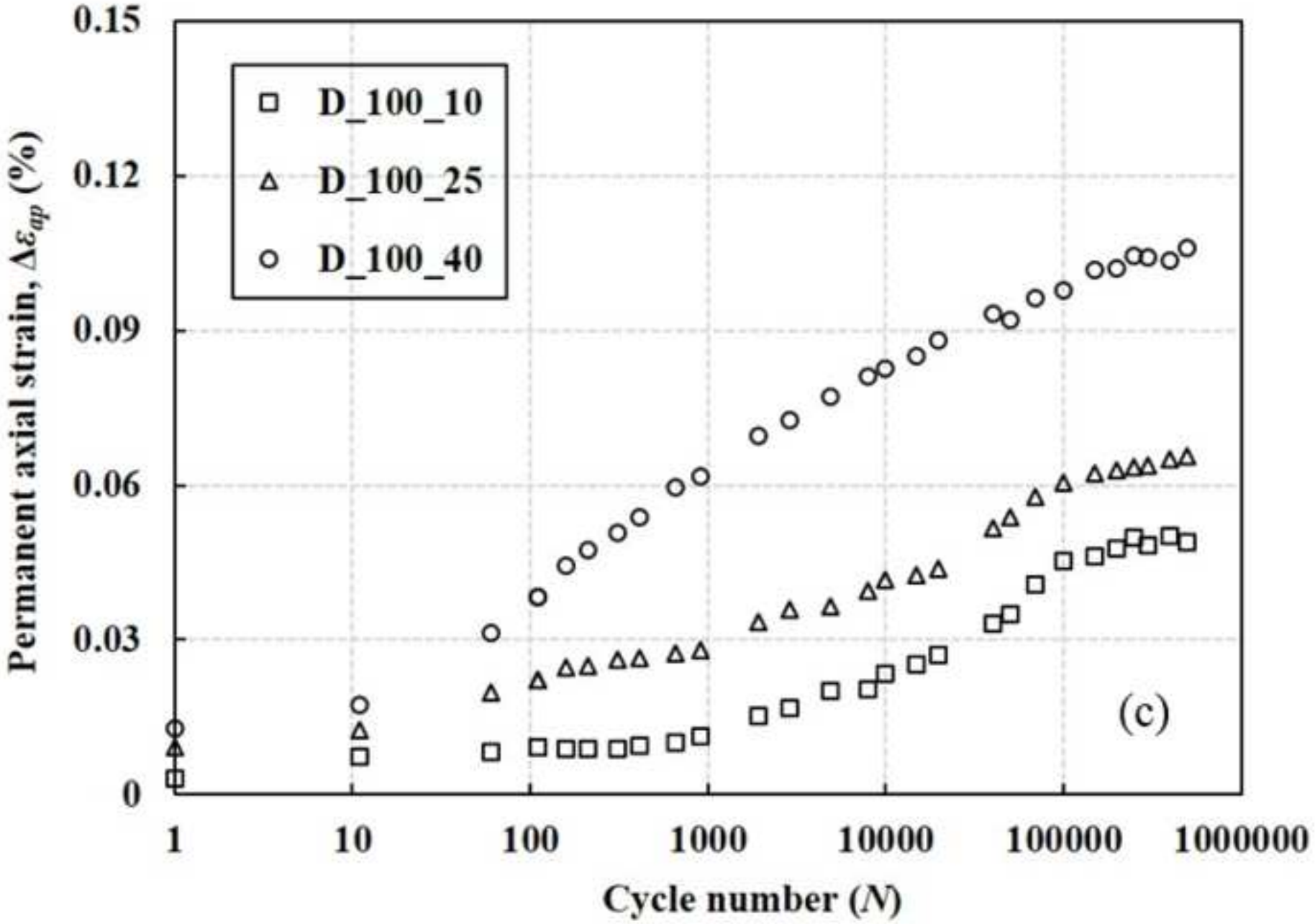

Figure 8

Click here to download Figure Figure 8.tif

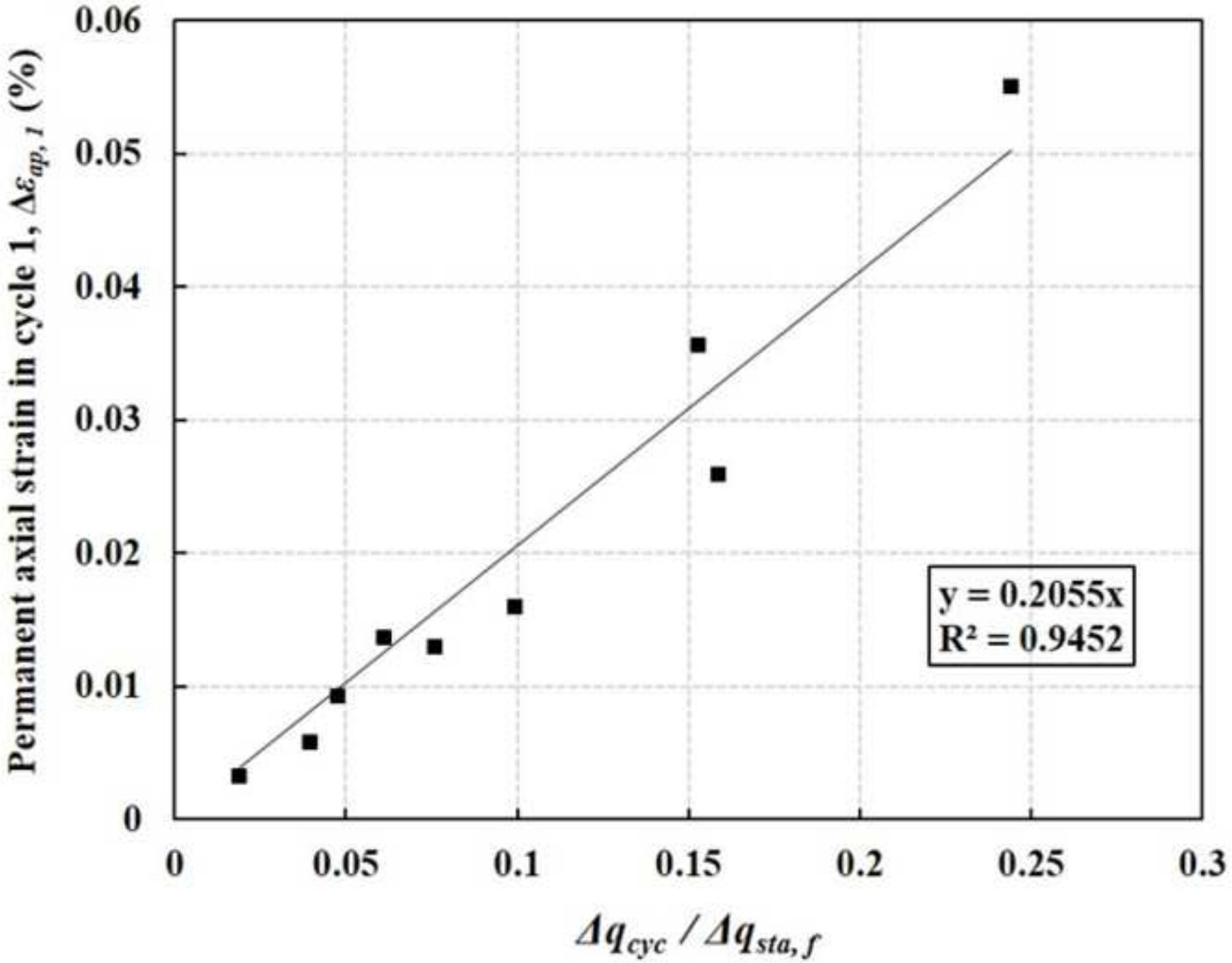

Figure 9

Click here to download Figure Figure 9.tif

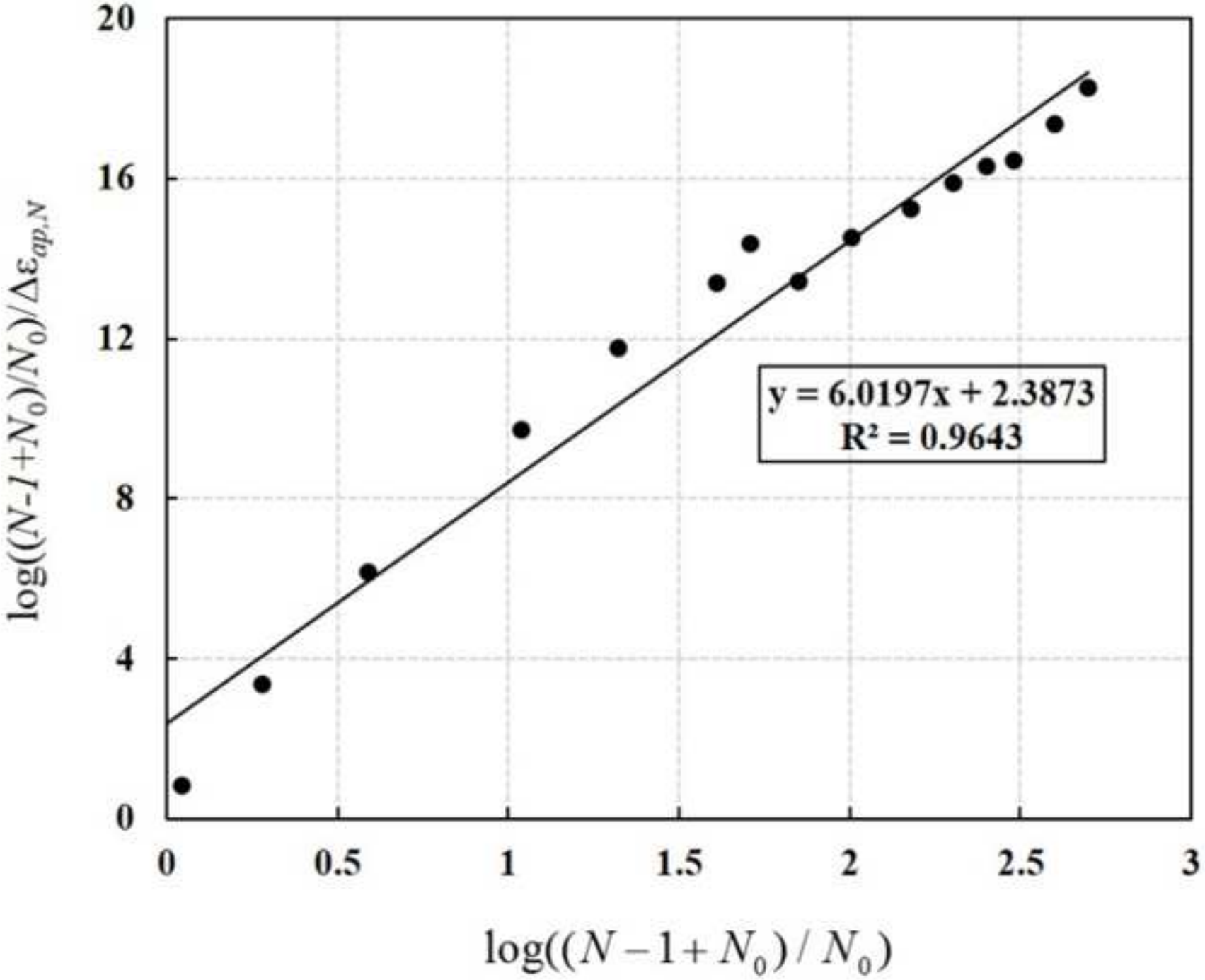

Figure 10 (a)

Click here to download Figure Figure 10 (a).tif

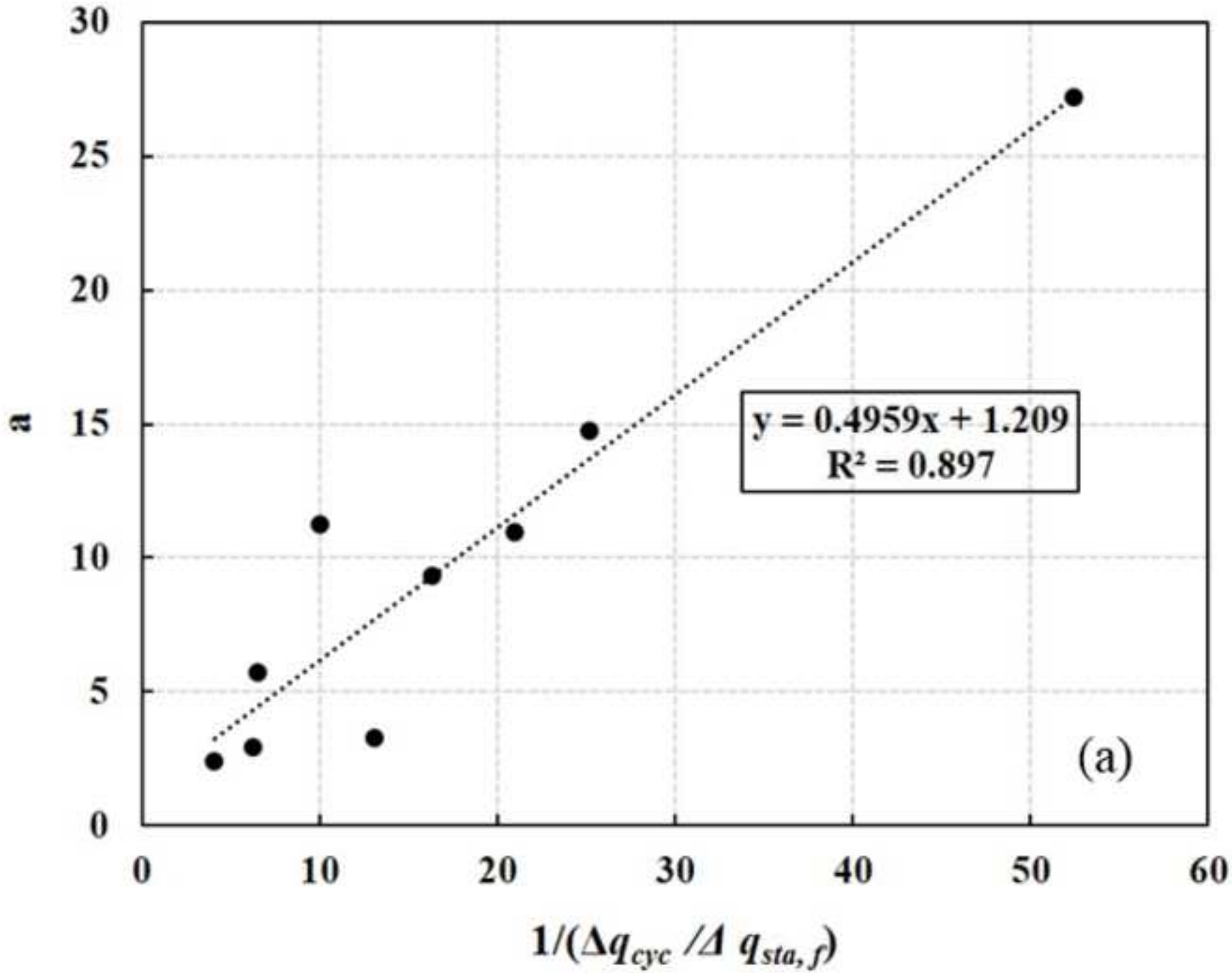

Figure 10 (b)

Click here to download Figure Figure 10 (b).tif

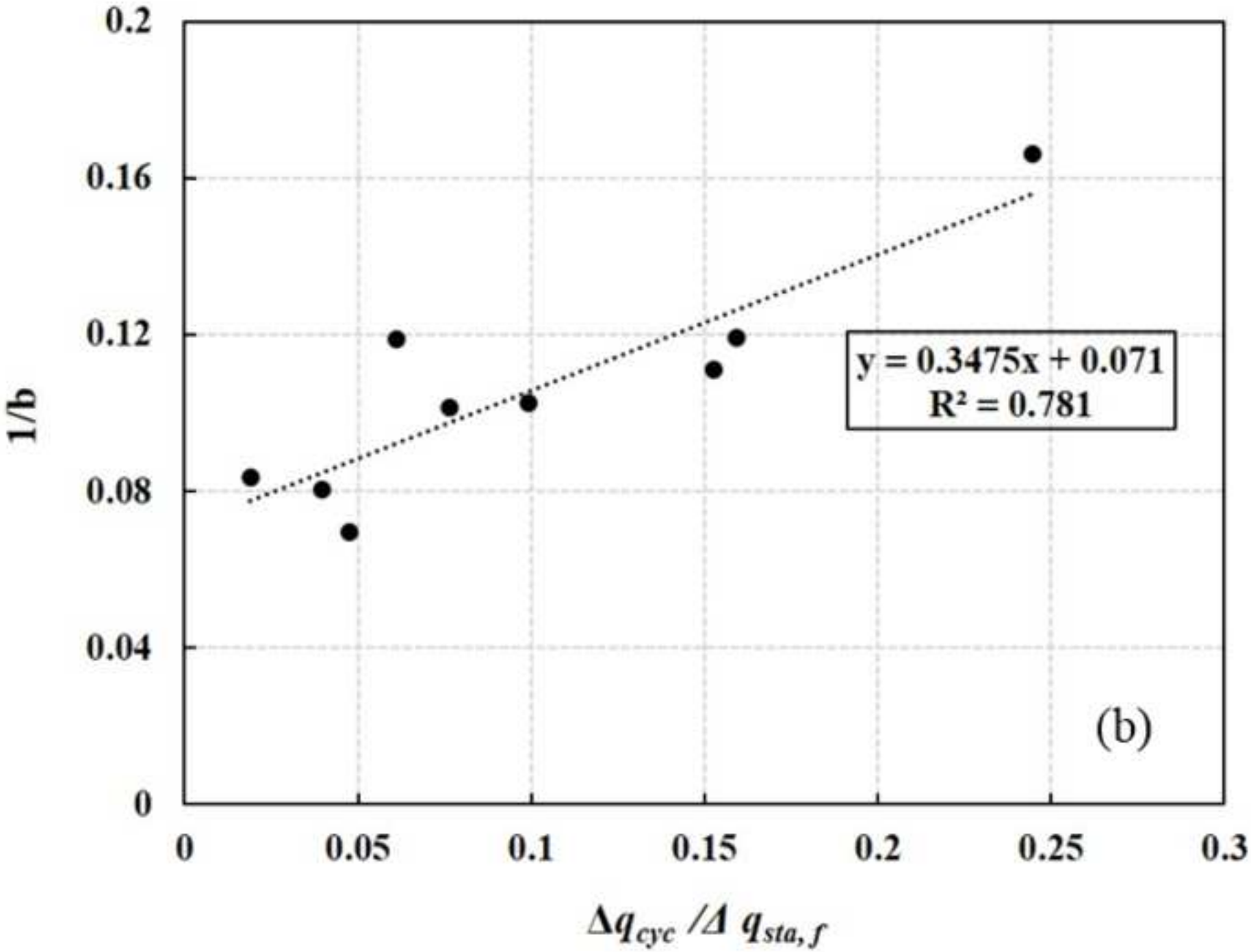

Figure 11 (a)

Click here to download Figure Figure 11 (a).tif

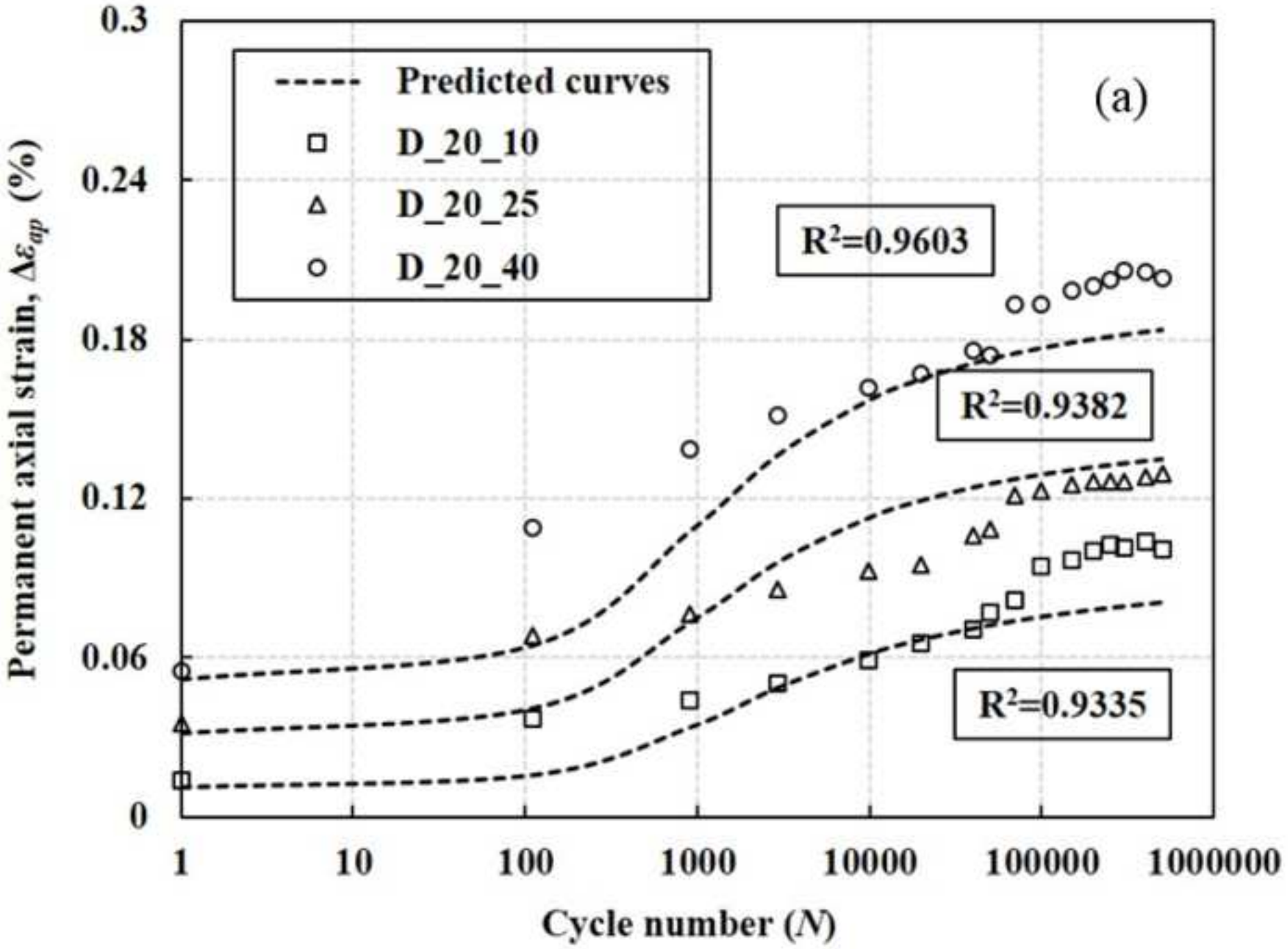

Figure 11 (b)

Click here to download Figure Figure 11 (b).tif

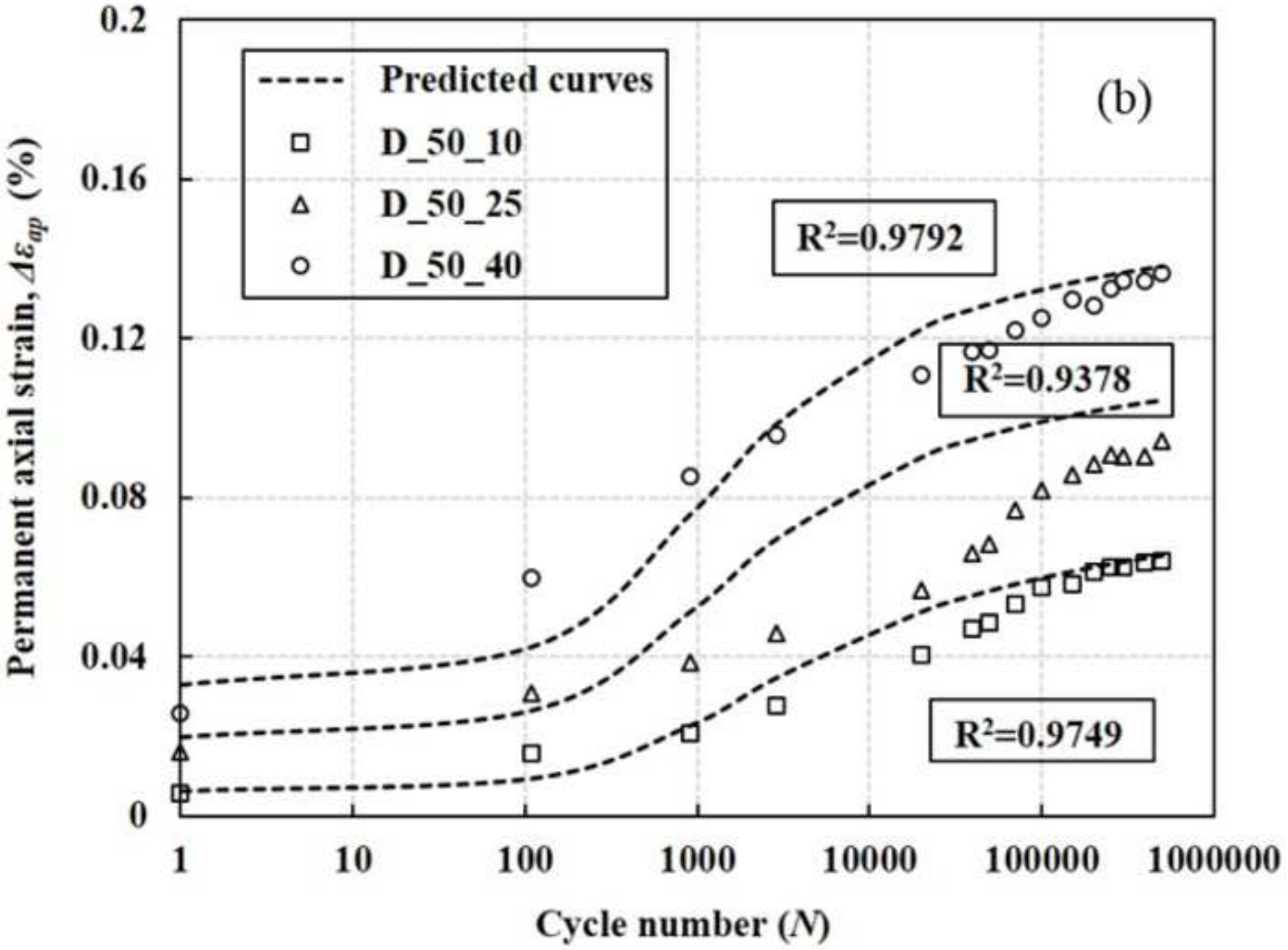

Figure 11 (c)

Click here to download Figure Figure 11 (c).tif

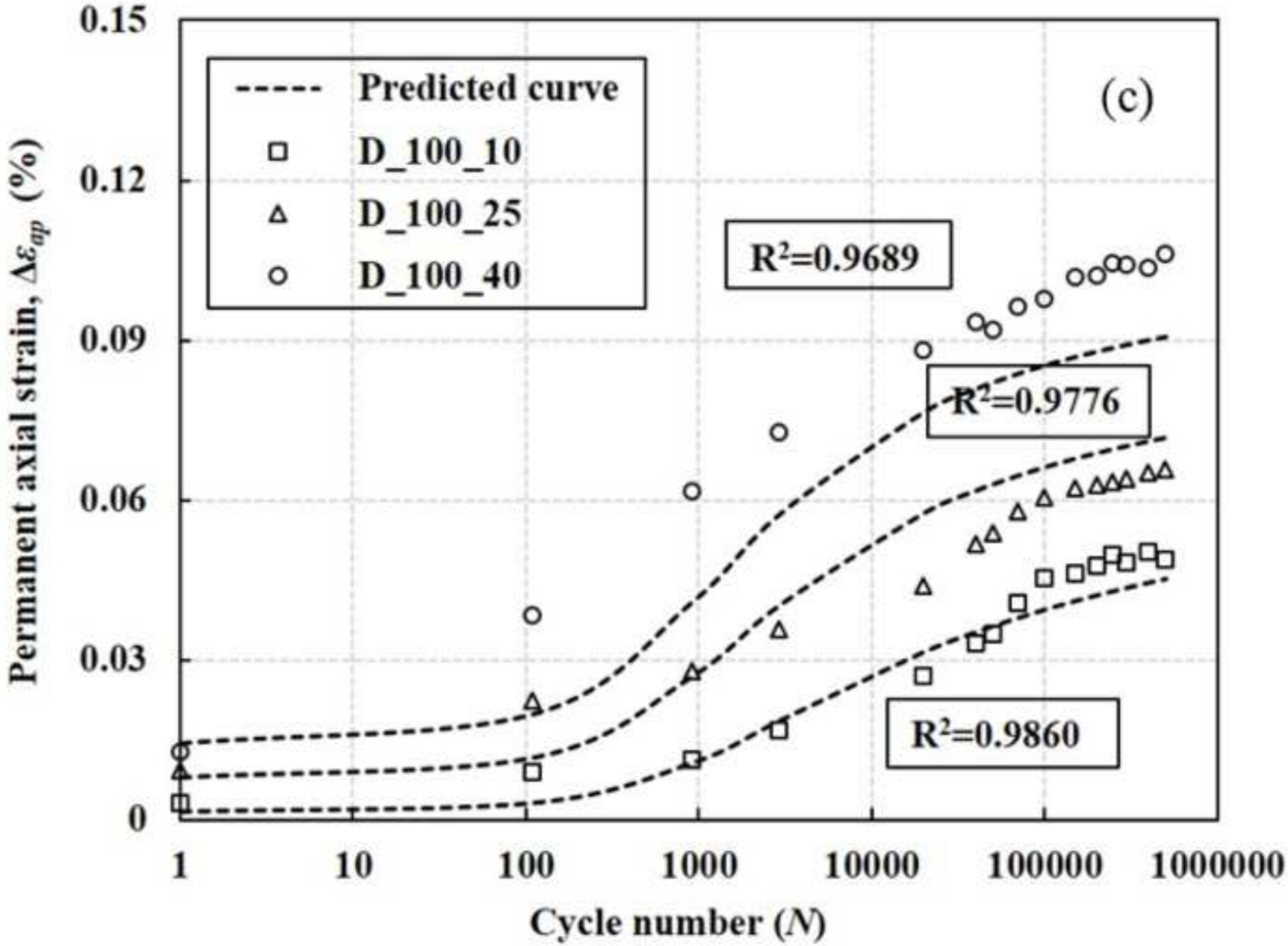

Figure 12 (a)

Click here to download Figure Figure 12 (a).tif

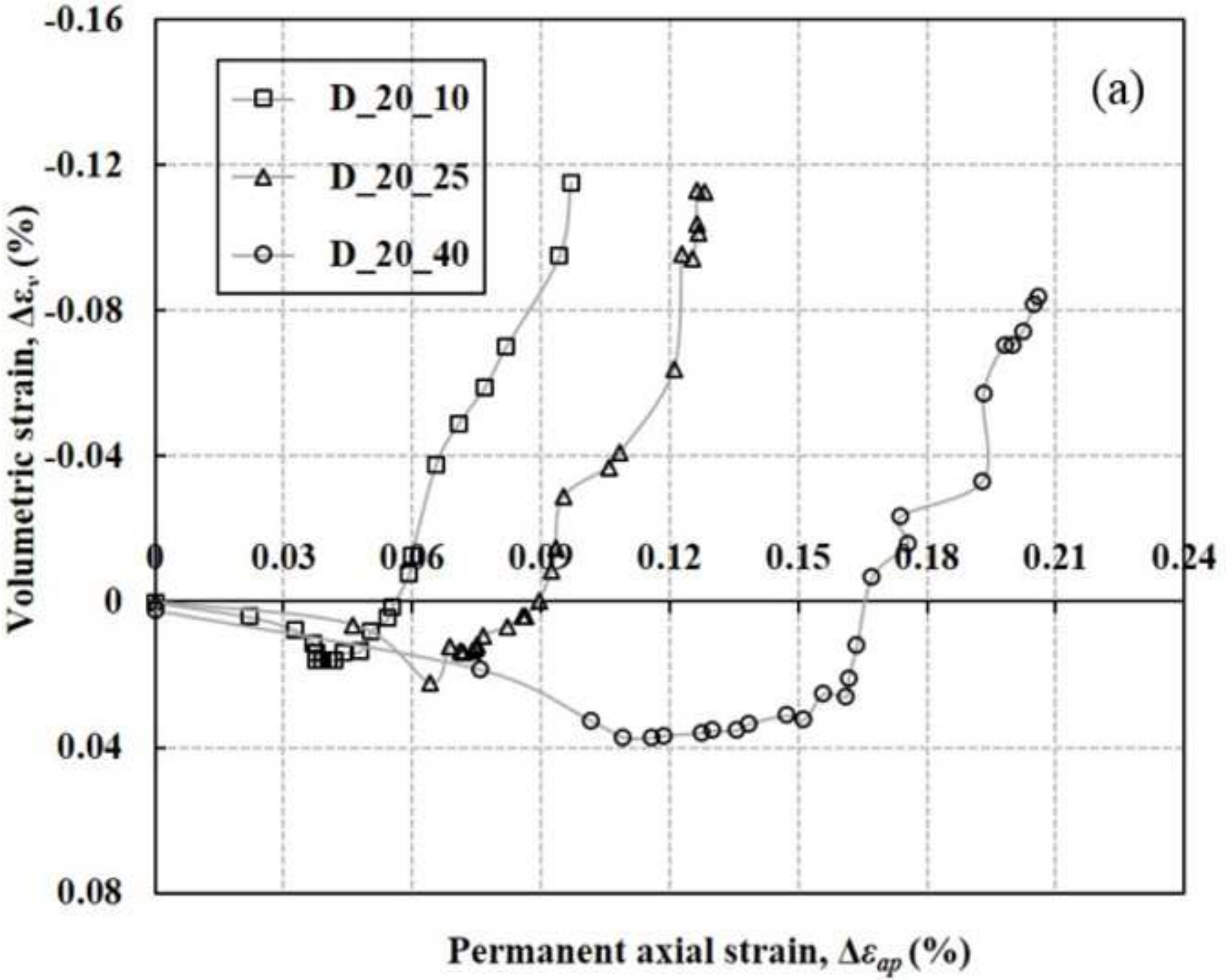

Figure 12 (b)

Click here to download Figure Figure 12 (b).tif

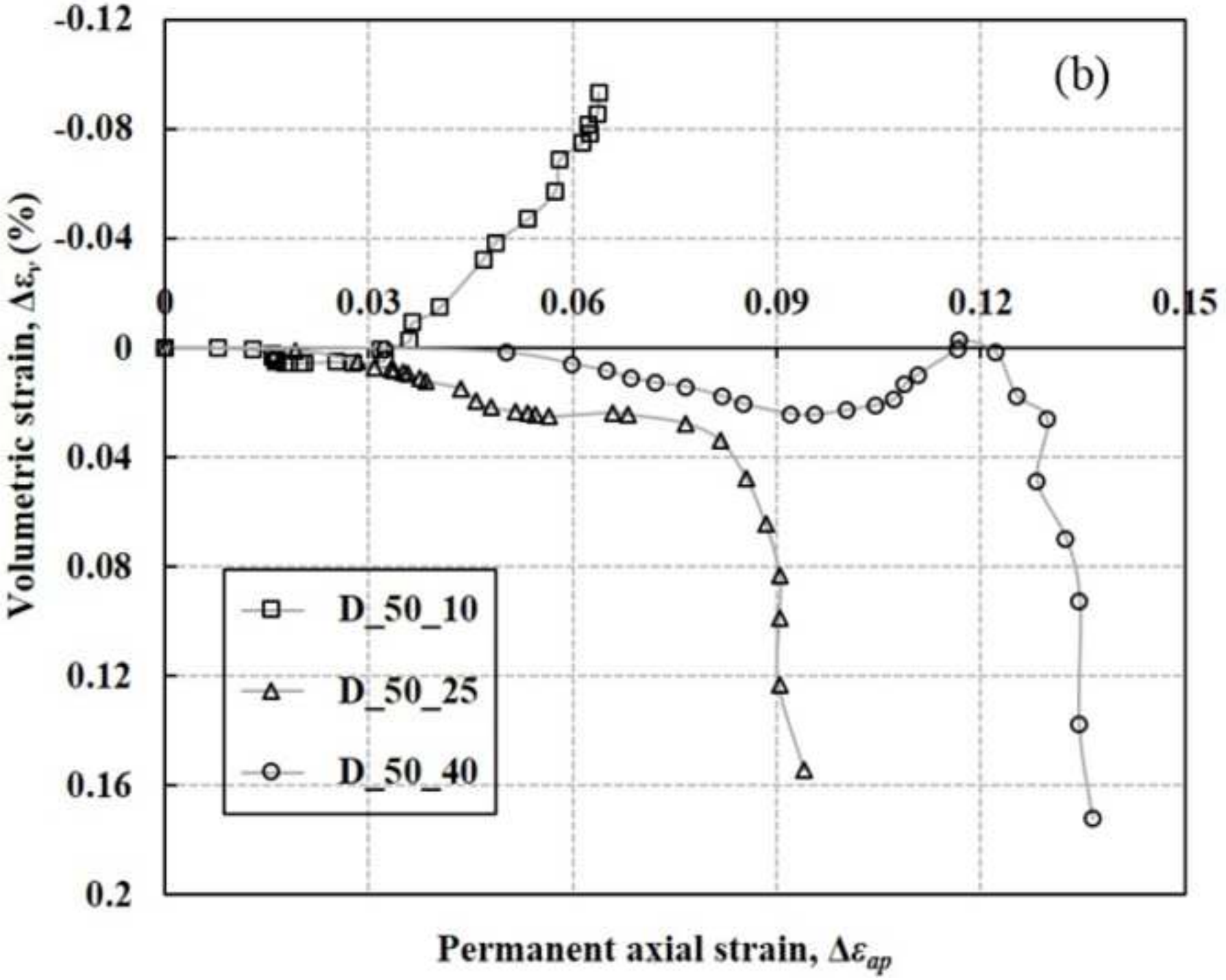

Figure 12 (c)

Click here to download Figure Figure 12 (c).tif

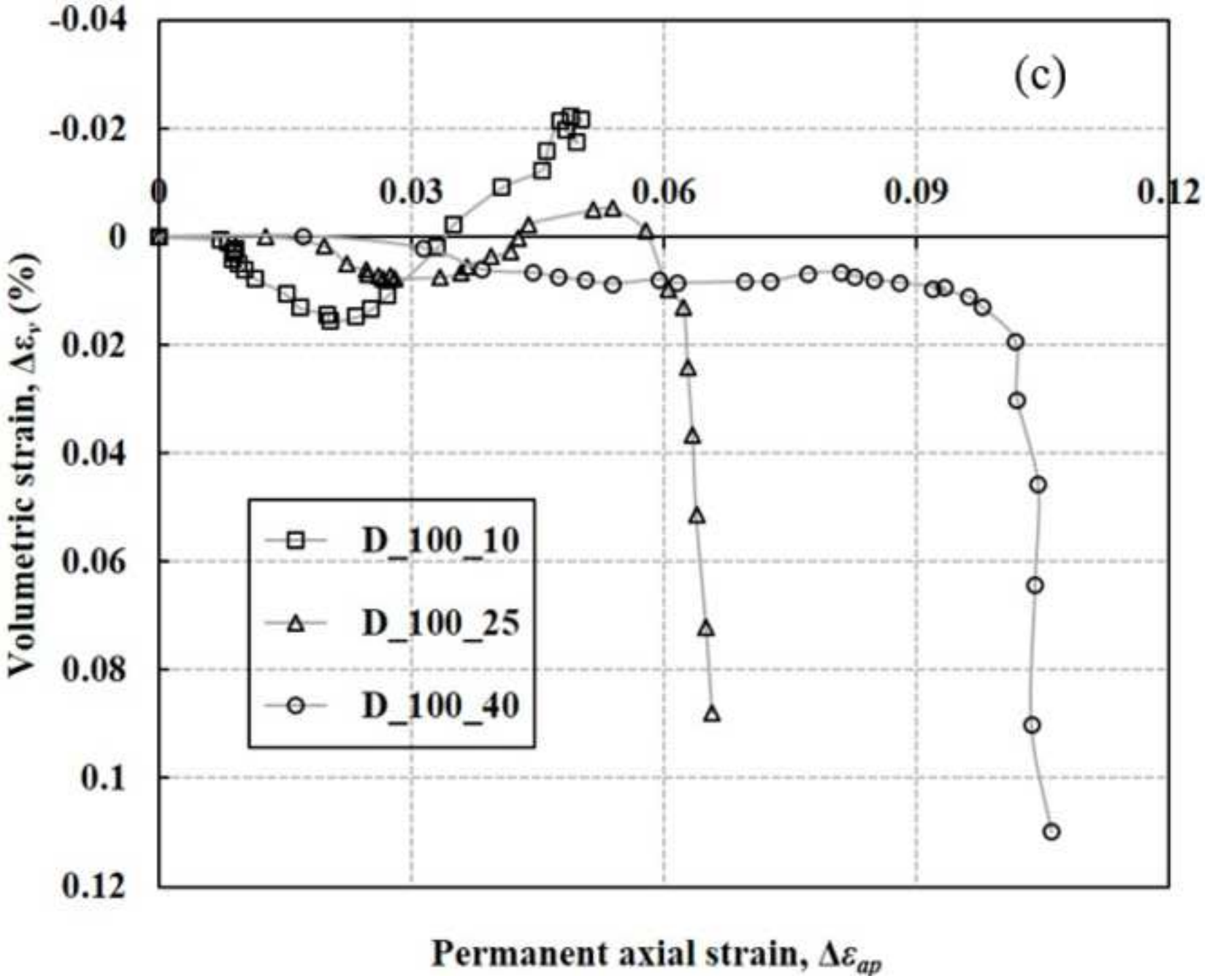

Figure 13

Click here to download Figure Figure 13.tif

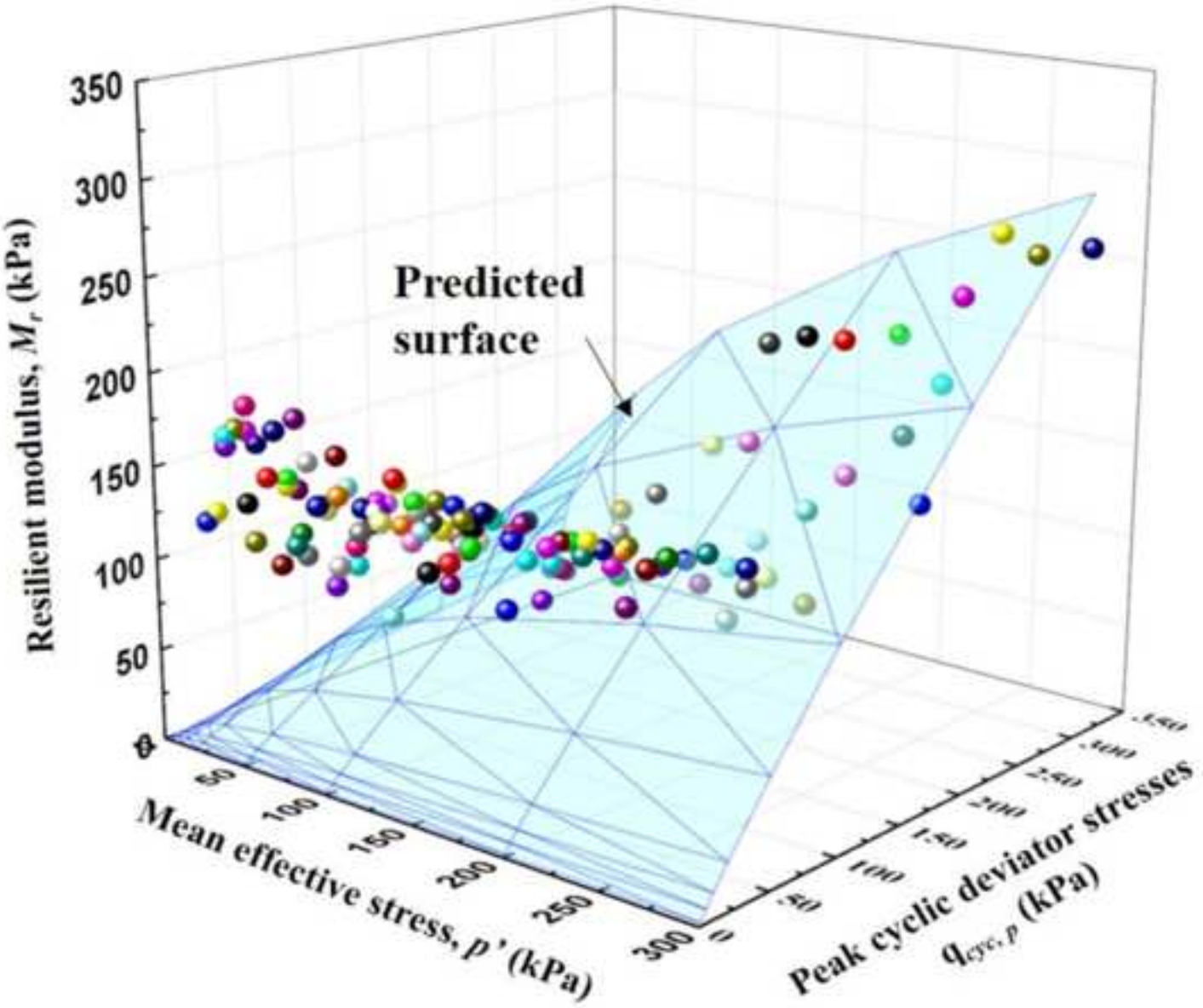

Figure 6 (d)

Click here to download Figure Figure 6 (d).tif

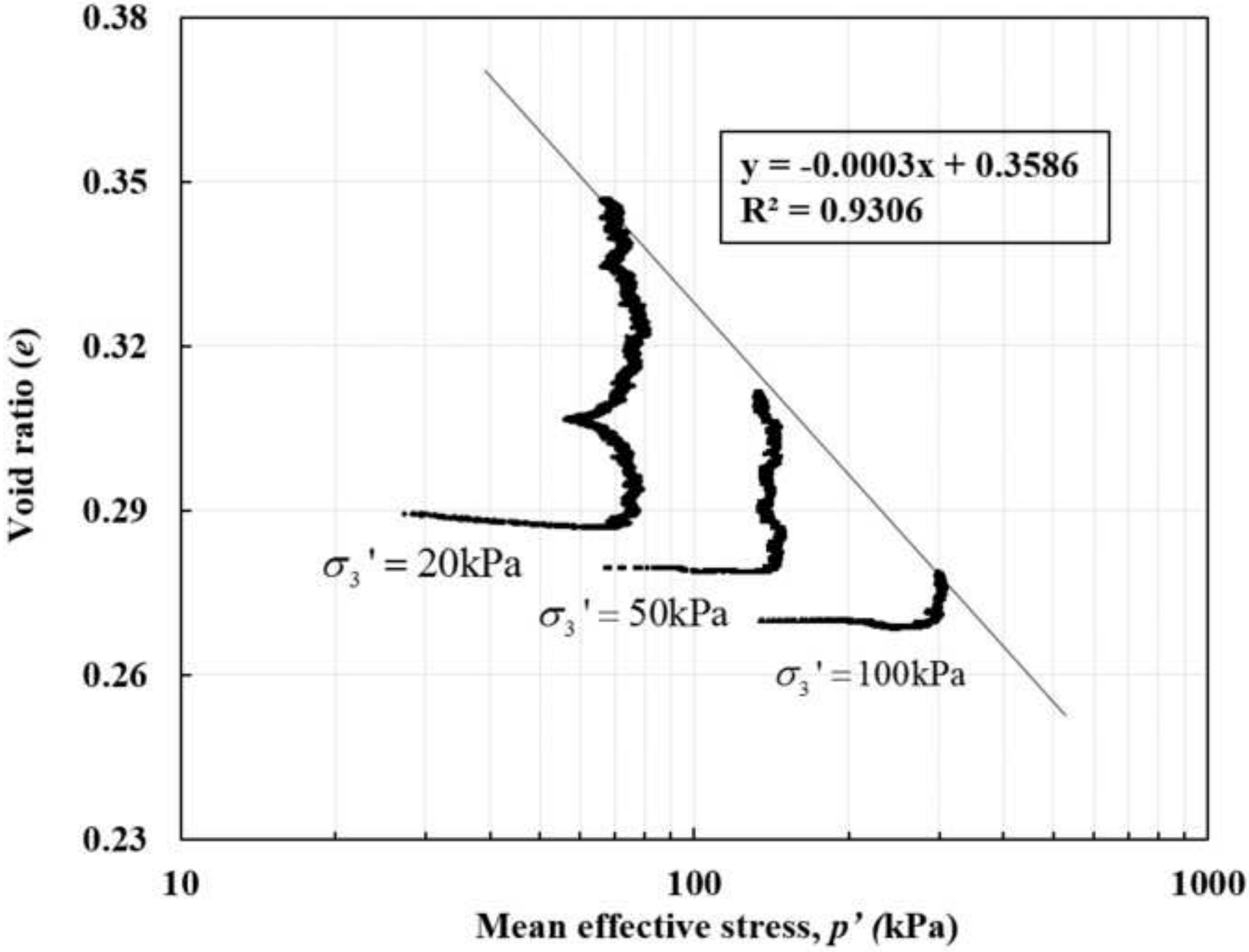

# Figure Captions List

Figure 1. Standard cross-section drawing of the HSR track bed and foundation of one-way ballastless track system and subgrade used in China

Figure 2. The original and the scaled-down particle size distribution curves

Figure 3. The sketch of stress path and the definitions of the variables under the same constant effective confining stress

Figure 4. The values and sequence of various consolidation stress states for RM_Sat specimen

Figure 5. The photos of the tested specimens: (a) after consolidation, (b) after static compression test, and (c) after cyclic loading test

Figure 6. (a) The plot of deviator stress ($q$) versus axial strain ($\varepsilon_a$) under three effective confining pressures, (b) The plot of mean effective stress ($p'$) versus deviator stress ($q$), (c) The plot of the stress ratio ($q/p'$) versus axial strain ($\varepsilon_a$), (d) The plot of the void ratio versus the logarithmic value of mean effective stress, all under static loading

Figure 7. The plots of permanent axial strain ($\Delta\varepsilon_{ap}$) versus the logarithmic cycle number ($N$) under three cyclic deviator stresses (10, 25 40 kPa) and three effective confining pressures (a) 20 kPa, (b) 50 kPa, and (c) 100 kPa

Figure 8. The plot of the permanent axial strain ( $\Delta\varepsilon_{ap,1}$ ) in cycle 1 versus $\Delta q_{cyc} / \Delta q_{sta,f}$

Figure 9. The original data of specimen D_20_40 and the curve fitting by a straight line

Figure 10. (a) The plot of the "a" value of each specimen versus $1/(\Delta q_{cyc} / \Delta q_{sta,f})$ and the fitting straight line, (b) the plot of the "1/b" value of each specimen versus $\Delta q_{cyc} / \Delta q_{sta,f}$ and the fitting straight line

Figure 11. The plots of permanent axial strain ($\Delta\varepsilon_{ap}$) versus cycle number ($N$) under three cyclic deviator stresses (10, 25 40 kPa) and three effective confining pressures (a) 20 kPa, (b) 50 kPa, and (c) 100 kPa and the predicted curves

Figure 12. The plots of volumetric strain ($\Delta\varepsilon_v$) versus axial strain ($\Delta\varepsilon_{ap}$) under three cyclic deviator stresses (10, 25 40 kPa) and under three effective confining pressures of (a) 20 kPa, (b) 50 kPa, and (c) 100 kPa

Figure 13. The plot of the resilient modulus ($M_r$) versus various peak cyclic deviator stresses ($q_{cyc,p}$)